Fuel 375 (2024) 131967

Contents lists available at ScienceDirect

Fuel

journal homepage: www.elsevier.com/locate/fuel

Full length article

Devolatilisation of beech wood char: Kinetics from thermogravimetric analyses and drop-tube reactor experiments

Maximilian Dammann [a,b,c,*,1], Stella Clara Walker [a,b], Marco Mancini [c], Thomas Kolb [a,b]

[a] Karlsruhe Institute of Technology (KIT), Engler-Bunte-Institute, Fuel Technology (EBI ceb), Engler-Bunte-Ring 1, 76131 Karlsruhe, Germany
[b] Karlsruhe Institute of Technology (KIT), Institute for Technical Chemistry, Gasification Technology (ITC vgt), Herrmann-von-Helmholtz-Platz 1, 76344 Eggenstein-Leopoldshafen, Germany
[c] Clausthal University of Technology, Institute for Energy Process Engineering and Fuel Technology (IEVB), Agricolastrasse 4, 38678 Clausthal-Zellerfeld, Germany

ARTICLE INFO

Keywords:
Devolatilisation
Wood char
Thermogravimetric
Drop tube
Kinetics

ABSTRACT

Reliable devolatilisation kinetics of primary wood chars are essential to describe the secondary release of volatiles in entrained flow gasification processes but have not been derived yet. Therefore, this study developed devolatilisation kinetics of a commercially available beech wood char using thermogravimetric analyses and drop-tube reactor experiments for design of entrained flow gasification processes. The thermogravimetric analyses were performed at low heating rates (2/5/10/30/50 K/min) up to 1273 K, whereas the drop-tube reactor experiments were conducted at high heating rates (~ 10^4 K/s), high temperatures (1273/1373/1473/1573/1673/1873 K) and short residence times (200/400 ms). Thermogravimetric kinetics were subsequently obtained based on multi first-order reaction logistic distributed activation energy models, while kinetics based on single first-order reaction Arrhenius law and modified Yamamoto models were derived from the drop-tube reactor experiments and corresponding CFD predictions. Finally, single-particle simulations were carried out to compare the kinetics from both kind of experiments at high-heating-rate conditions. The comparisons demonstrate that the thermogravimetric kinetics are in reasonable agreement with the drop-tube reactor kinetics but provide lower devolatilisation rates. Furthermore, gas species concentrations measurements from the drop-tube reactor experiments were used to estimate an average volatiles composition. The results indicate that the volatiles composition at high-temperature conditions can likely be described using the gas species concentrations at high-temperature equilibrium conditions.

1. Introduction

Primary wood chars are the solid residues of the thermal decomposition of woody biomass under inert conditions using moderate temperatures of up to 900 K. Such chars can be mixed with pyrolysis oils to energy-rich slurries to obtain feedstocks for the production of liquid fuels and chemicals in closed carbon cycle economies [2]. Specifically, primary wood chars can be converted via several physical and thermo-chemical process steps to synthesis gas in entrained flow gasification processes with typical process temperatures above 1500 K. These process steps include drying, devolatilisation due to incomplete primary pyrolysis, fragmentation, heterogeneous gasification and mineral matter transformation, where devolatilisation and heterogeneous gasification are typically considered as consecutive process steps (see [3–5]) and described using separate kinetics. As such kinetics are essential for the numerical design and scale-up of gasification processes, numerous studies already focussed on heterogeneous gasification kinetics of biomass chars (see [6]), pyrolysis of raw biomass (see Table S1) or network devolatilisation models for raw biomass (see bioFlashchain [7–10], bio-CPD [11], bio-FG DVC [12] or FG-BioMass [13]). In particular, several studies addressed the heterogeneous gasification of chars that were produced using secondary pyrolysis of primary chars (in analogy to the process step in entrained flow gasification) and are also referred as secondary chars. For example, Stösser et al. [14,15] and Schneider et al. [16,17] developed intrinsic secondary wood char kinetics for reactions with carbon dioxide and water vapour.

Furthermore, Simone et al. [18], Niemelä et al. [19] and Johansen et al. [20–22] applied combined experimental and numerical research to derive devolatilisation kinetics of raw biomass. Simone et al. [18] determined two-stage (low-temperature and medium-temperature) single first-order devolatilisation kinetics for biomass, based on inert DTR experiments between 673 K and 1073 K and based on corresponding CFD simulations. The experimental conversion was obtained using the ash-tracer method, while the CFD simulations relied on assumed

* Corresponding author.
[1] ORCID: http://orcid.org/0000-0002-2851-7787.

https://doi.org/10.1016/j.fuel.2024.131967
Received 30 July 2023; Received in revised form 15 May 2024; Accepted 16 May 2024
Available online 23 July 2024

Nomenclature

Latin symbols

Bi	Biot number
C	coefficient
d	diameter
$\overline{E}_a$	molar activation energy
$\overline{\boldsymbol{E}}_a$	molar activation energy vector
f	probability density function
F	modification factor
k	rate constant
k_0	pre-exponential factor
$\boldsymbol{k}_0$	pre-exponential factor vector
m	mass
$\dot{m}$	mass flow rate
M	molar mass
N	number of parallel reactions
$\dot{N}$	number flow rate
p	pressure
r	centre distance
r	volume fraction
R	reaction rate
R	residual
R^2	coefficient of determination
$\overline{R}$	molar gas constant
t	time
T	temperature
$\dot{V}$	volume flow rate
w	mass fraction
$\boldsymbol{w}$	mass fraction vector
x	mole fraction
$\boldsymbol{x}$	mole fraction vector
X	conversion
z	distance from dosing tube inlet

Greek symbols

β	heating rate
μ	expectation
$\boldsymbol{\mu}$	expectation vector
ρ	density
σ	standard deviation
$\boldsymbol{\sigma}$	standard deviation vector

Subscripts and superscripts

asr	on as-received basis
bal	balanced
calc	calculated
cg	of the carrier gas stream
comb	of the combustibles/fixed carbon
d	on dry basis
dev	devolatilisation
dry gas,out	of the dry gas stream at outlet
$\overline{E}_a$	of the logistic distribution for the molar activation energy
eq	at equilibrium conditions
eqd	equilibrium-derived
eqd,C	equilibrium-derived, based on carbon balancing
eqd,H	equilibrium-derived, based on hydrogen balancing
eqd,O	equilibrium-derived, based on oxygen balancing
gas	gas
gas,in	of the gas stream at inlet
i	of reaction i, of element i
iwc	of the intermediate wood char
j	of element j
max	maximum
meas	measured
min,dev	minimum after complete devolatilisation
MYM	of the modified Yamamoto model
op	operating
part	particle
pwc	of the primary wood char
res	residence
rs	of the remaining sample
rlv	of the released volatiles
rv	of the remaining volatiles
SFORALM	of the single first-order reaction Arrhenius law model
sg	of the secondary gas stream
sim	simulated
STP	at standard conditions according to ISO 10780:1994 [1]
swc	of the secondary wood char
tot	total
vol	of/in the volatiles
0	initial

Acronyms

CFD	computational fluid dynamics
DTG	differential thermogravimetric
DTR	drop-tube reactor
HHV	higher heating value
LHV	lower heating value
MFORLDAEM	multi first-order reaction logistic distributed activation energy model
MYM	modified Yamamoto model
RD	relative deviation
SFORALM	single first-order reaction Arrhenius law model
STP	at standard conditions according to ISO 10780:1994 [1]
TG	thermogravimetric

wall temperatures as boundary conditions for the solution of the energy equation. Niemelä et al. [19] carried out DTR experiments at 873 K and 1173 K under inert atmosphere to obtain single-first order devolatilisation kinetics for three particle size fractions of biomass between 93 µm and 1358 µm. Particle mass loss, wall temperature, particle velocity and particle density measurements were performed to determine the experimental conversion, the wall boundary conditions, the particle shape factor (the ratio of the surface area of a spherical volume-equivalent particle to the real surface area) and the effective particle density, respectively. Finally, a CFD based optimisation was

performed using the measured particle size distributions and neglecting the internal particle temperature gradients. Johansen et al. [20–22] applied devolatilisation experiments in a laminar entrained flow reactor with peak temperatures between 1405 K and 1667 K and a CFD based optimisation, similar to Niemelä et al. [19], to obtain single first-order devolatilisation kinetics for biomass. In a first iteration, the particle size distribution was approximated using the Rosin-Rammler distribution, and internal temperature gradients were neglected. In a second iteration, the influence of internal particle temperature gradients on both kinetics and conversion were investigated to determine temperature corrected devolatilisation kinetics for CFD simulations. The developed method avoided overestimation of conversion times by 80-90% compared to the initial results.

Finally, two studies [15,23] only investigated devolatilisation kinetics of primary wood chars. Branca and Di Blasi [23] developed devolatilisation kinetics for several chars at thermogravimetric (TG) combustion conditions with temperatures of up to 873 K using multi-reaction Arrhenius law models. Stösser [15] performed inert high-temperature drop-tube reactor (DTR) experiments with fir char (containing more than 25% volatiles) and established devolatilisation kinetics based on a single first-order reaction Arrhenius law model. However, the devolatilisation kinetics of both studies have significant deficiencies for the numerical design and scale-up of entrained flow gasifiers, as Branca and Di Blasi [23] performed their experiments in oxidative atmosphere to describe both char devolatilisation and char oxidation and Stösser [15] neglected the impact of the particle size distribution and the strongly changing gas conditions. Reliable devolatilisation kinetics have thus not been developed yet for wood chars to the best knowledge of the authors. However, such kinetics, together with heterogeneous gasification kinetics, are decisive for the numerical design and scale-up of entrained flow gasification processes, as both devolatilisation and heterogeneous gasification strongly affect the conversion and the far-flame process conditions (see [5]). Therefore, this study is focussed on the development of devolatilisation kinetics for beech wood char at atmospheric high-temperature conditions using data from TG analyses and DTR experiments. Firstly, TG analyses were performed at inert atmospheric conditions to determine devolatilisation kinetics for low-heating rate conditions. Secondly, secondary pyrolysis experiments were carried out at various operating temperatures and various operating residence times in a drop-tube reactor to establish devolatilisation kinetics for high-heating rate conditions. Following previous studies [18–23], combined experimental and numerical approaches were used to derive and compare the kinetics. The experimental and mathematical methods are described in Section 2 while the results of the TG analyses and DTR experiments are presented in Section 3 and are discussed in Section 4. The conclusions are given in Section 5.

2. Methods

This section describes the experimental and mathematical methods that were used to derive devolatilisation kinetics of primary beech wood char from thermogravimetric analyses (TG kinetics) and drop-tube reactor experiments (DTR kinetics).

2.1. Preparation

Beech wood char, originally produced by Holzkohlenverarbeitung Schütte [24] at moderate temperatures of 800–900 K, was previously applied as feedstock for atmospheric and high-pressure entrained flow gasification experiments [5,25]. Sample material from this feedstock was sieved to 50–150 µm using an oscillating screening machine (GKM Siebtechnik), as another intention was to investigate the reactivity of the secondary wood chars with particle sizes ranging from 50 µm to 100 µm in subsequent studies [17,26] anticipating fragmentation in the course of secondary pyrolysis experiments. Specifically, the sieving was carried out to remove the smaller particles possibly characterised by higher ash contents and the larger particles typically affected by higher temperature gradients during the heat-up [26]. In order to avoid agglomeration, the sample material was dried for at least 12 h at 378 K and sieved batchwise covering the sieves with thin layers of particles. The dried sieved sample material was applied in both the TG analyses and the DTR experiments.

2.2. Chemical analyses

Proximate, ultimate and heating value analyses of the unsieved samples and the samples used in the TG analyses were performed based on DIN 51732:2007 [27], DIN 51724-3:2012 [28], DIN 51719:1997 [29], DIN 51718:2002 [30], DIN 51720:2001 [31] and DIN 51900-2:2003 [32] at the laboratory of Eurofins [33].

Proximate and ultimate analyses of the samples used or collected in the DTR experiments were carried out according to DIN EN 15104:2011 [34], DIN EN 15289:2011 [35], DIN 51719:1997 [29], DIN 51718:2002 [30] and DIN 51720:2001 [31] at the laboratory of Engler-Bunte-Institute of Karlsruhe Institute of Technology.

Oxygen contents of the samples were determined by difference, while equilibrium elemental, equilibrium fixed carbon and equilibrium volatiles contents of the dry samples were calculated with Python and Cantera [36] using the minimisation of the Gibbs energy at 1873 K and 1 bar and accounting for C(gr), CH_4, CO, CO_2, H_2 H_2O, O_2 and N_2 as possible species.

Furthermore, devolatilisation conversions were derived for the samples collected in the DTR experiments from the measured carbon, hydrogen and oxygen contents using equilibrium calculations and balancing. The devolatilisation conversions are hereinafter referred as (mean) equilibrium-derived devolatilisation conversions $X_{\mathrm{dev,eqd}}$ and were determined in three steps. Firstly, it is assumed that, on dry basis, the elemental content of a collected secondary wood char sample approximately corresponds to the equilibrium-derived elemental content of the wood char sample at a specific devolatilisation conversion. Specifically, $w_{i,\mathrm{swc,d}} \approx w_{i,\mathrm{iwc,d,eq}}\left(X_{\mathrm{dev,eqd},i}\right)$ is assumed for element i, where $w_{i,\mathrm{swc,d}}$ is the elemental mass fraction in the collected secondary wood char on dry basis, $w_{i,\mathrm{iwc,d,eq}}$ is the equilibrium elemental mass fraction in the intermediate wood char on dry basis and $X_{\mathrm{dev,eqd},i}$ is the corresponding equilibrium-derived devolatilisation conversion. The equilibrium elemental mass fractions in the intermediate wood char on dry basis $\boldsymbol{w}_{\mathrm{iwc,d,eq}} = \left(w_{i,\mathrm{iwc,d,eq}}\right)$ are given by

$$w_{i,\mathrm{iwc,d,eq}} = \frac{w_{i,\mathrm{pwc,d,eq}} - w_{i,\mathrm{vol,eq}}\, w_{\mathrm{vol,pwc,d,eq}}\, X_{\mathrm{dev,eqd},i}}{\sum_j w_{j,\mathrm{pwc,d,eq}} - w_{j,\mathrm{vol,eq}}\, w_{\mathrm{vol,pwc,d,eq}}\, X_{\mathrm{dev,eqd},i}}, \tag{1}$$

where $w_{i,\mathrm{vol,eq}}$ and $w_{j,\mathrm{vol,eq}}$ are the equilibrium mass fractions of *element* i and j, respectively, in the volatiles and $w_{i,\mathrm{pwc,d,eq}}$, $w_{j,\mathrm{pwc,d,eq}}$ and $w_{\mathrm{vol,pwc,d,eq}}$ are the equilibrium mass fractions of element i, element j and the volatiles, respectively, in the primary wood char on dry basis. The equilibrium mass fractions of the *elements* in the volatiles are given by

$$w_{\mathrm{C,vol,eq}} = M_{\mathrm{C}}\left(\frac{w_{\mathrm{CH_4,vol,eq}}}{M_{\mathrm{CH_4}}} + \frac{w_{\mathrm{CO,vol,eq}}}{M_{\mathrm{CO}}} + \frac{w_{\mathrm{CO_2,vol,eq}}}{M_{\mathrm{CO_2}}}\right), \tag{2}$$

$$w_{\mathrm{H,vol,eq}} = M_{\mathrm{H}}\left(4\cdot\frac{w_{\mathrm{CH_4,vol,eq}}}{M_{\mathrm{CH_4}}} + 2\cdot\frac{w_{\mathrm{H_2,vol,eq}}}{M_{\mathrm{H_2}}} + 2\cdot\frac{w_{\mathrm{H_2O,vol,eq}}}{M_{\mathrm{H_2O}}}\right), \tag{3}$$

$$w_{\mathrm{O,vol,eq}} = M_{\mathrm{O}}\left(\frac{w_{\mathrm{CO,vol,eq}}}{M_{\mathrm{CO}}} + 2\cdot\frac{w_{\mathrm{CO_2,vol,eq}}}{M_{\mathrm{CO_2}}} + \frac{w_{\mathrm{H_2O,vol,eq}}}{M_{\mathrm{H_2O}}}\right), \tag{4}$$

$$w_{\mathrm{N,vol,eq}} = M_{\mathrm{N}}\left(2\cdot\frac{w_{\mathrm{N_2,vol,eq}}}{M_{\mathrm{N_2}}}\right), \tag{5}$$

where $w_{\mathrm{CH_4,vol,eq}}$, $w_{\mathrm{CO,vol,eq}}$, $w_{\mathrm{CO_2,vol,eq}}$, $w_{\mathrm{H_2,vol,eq}}$, $w_{\mathrm{H_2O,vol,eq}}$ and $w_{\mathrm{N_2,vol,eq}}$ are the equilibrium mass fractions of the species in the volatiles and M_{C}, $M_{\mathrm{CH_4}}$, M_{CO}, $M_{\mathrm{CO_2}}$, M_{H}, $M_{\mathrm{H_2}}$, $M_{\mathrm{H_2O}}$, M_{O}, M_{N} and

M_{N_2} are molar masses. Secondly, the equilibrium-derived devolatilisations conversions based on carbon balancing $X_{dev,eqd,C}$, based on hydrogen balancing $X_{dev,eqd,H}$ and based on oxygen balancing $X_{dev,eqd,O}$ were calculated by

$$X_{dev,eqd,C} \in [0,1] \quad \text{such that} \quad w_{C,swc,d} \approx w_{C,pwc,d,eq}\left(X_{dev,eqd,C}\right), \tag{6}$$

$$X_{dev,eqd,H} \in [0,1] \quad \text{such that} \quad w_{H,swc,d} \approx w_{H,pwc,d,eq}\left(X_{dev,eqd,H}\right), \tag{7}$$

$$X_{dev,eqd,O} \in [0,1] \quad \text{such that} \quad w_{O,swc,d} \approx w_{O,pwc,d,eq}\left(X_{dev,eqd,O}\right). \tag{8}$$

Thirdly, (mean) equilibrium-derived devolatilisation conversions $X_{dev,eqd}$ were determined by

$$X_{dev,eqd} = \frac{1}{3}\sum_{i=C,H,O} X_{dev,eqd,i}\,. \tag{9}$$

2.3. Particle size distribution measurements

Particle size distributions were measured using laser diffraction (Sympatec HELOS H0309) at the Institute of Mechanical Process Engineering and Mechanics of Karlsruhe Institute of Technology. Mass-based probability density functions q_3 and cumulative distribution functions Q_3 were determined twice and averaged.

2.4. TG analyses

TG analyses were carried out using a commercial device (Netzsch TG 209 F1) at Engler-Bunte-Institute, Fuel Technology of Karlsruhe Institute of Technology (see [15,37]). First, dried wood char samples of 4.2–5.5 mg were filled into the Al_2O_3 crucibles of the device and flushed with nitrogen. Then, the samples were heated up at heating rates of 2 K/min, 5 K/min, 10 K/min, 30 K/min and 50 K/min up to a temperature of 1273 K. Nitrogen was used as inert gas applying volume flow rates (STP) of 35 l/min. The mass loss (TG) curves were continuously measured during the thermal treatment with a scanning frequency of 1 min^{-1}, while the DTG curves were obtained using derivation of the TG curves and subsequent cubic smoothing spline interpolation with the *csaps* method of Matlab [38]. The curves were determined twice for the heating rates of 2 K/min, 5 K/min, 10 K/min and 30 K/min and three times for the heating rate of 50 K/min and were subsequently averaged. The averaged TG curves provide the measured mass fraction of the remaining sample $w_{rs,meas}$ (also referred as the solid mass fraction). Furthermore, the TG curves were used to determine the measured mass fraction of the remaining volatiles $w_{rv,meas}$. Firstly, the curves were normalised with respect to the equilibrium-derived volatiles content of the primary wood char (batch TG) on dry basis $w_{vol,pwc,d,eq}$. The curves were obtained by

$$w_{rv,meas} = 1 - \frac{1 - w_{rs,meas}}{w_{vol,pwc,d,eq}}\,. \tag{10}$$

Secondly, the normalised curves were cut-off below a mass fraction of 12%, as the measurement data below this mass fraction could significantly overestimate the reactions rates (see Sections 3.3 and S4). It is assumed that the impact is significantly larger below the cut-off fraction than above the cut-off fraction. Moreover, the normalised curves can be used to derive the curves of the measured mass fraction of the released volatiles $w_{rlv,meas}$ (see [39]) given by

$$w_{rlv,meas} = 1 - w_{rv,meas}\,. \tag{11}$$

2.5. DTR experiments

DTR experiments were performed using the drop-tube reactor of Engler-Bunte-Institute, Fuel Technology of Karlsruhe Institute of Technology (see [14,15,26]) shown in Fig. 1 and described in Section S2. First, dried wood char particles were evacuated, flushed with nitrogen and fed to an argon stream using a speed-controlled scale and a hopper.

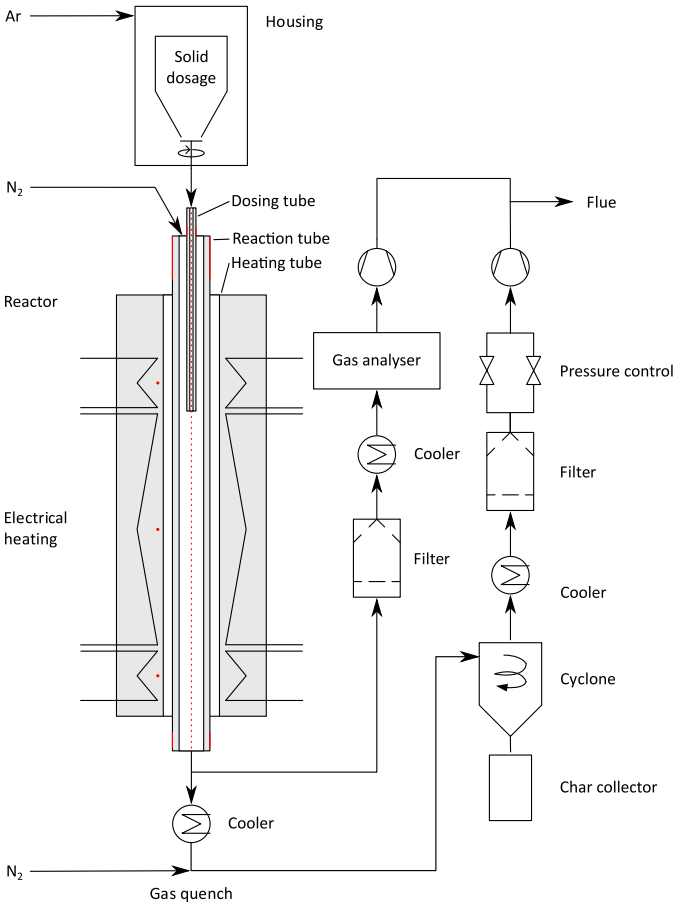

Fig. 1. Sketch of the DTR. Temperature measurement points and regions are marked with red colour.

Then, the carrier gas stream with the particles was supplied to the reactor through a dosing tube while a secondary gas stream containing nitrogen was fed to the reactor through an annular gap between dosing tube and reaction tube (see Fig. 1). Both gas streams were controlled using pre-calibrated mass flow controllers (Bronkhorst EL-Flow). At the outlet of the reaction tube, gas samples were extracted from the gas stream and were subsequently filtered, quenched and transferred to a micro gas chromatograph (Agilent Technologies 490 Micro GC), previously calibrated using reference gases. After the sample extraction, the gas stream was quenched to temperatures below 673 K by a cooler and nitrogen [26]. Finally, the gas stream successively passed a cyclone separator [26], a cooler and a candle filter (HEPA). The particles separated at the cyclone separator were collected in a nitrogen-flushed lock [26].

Furthermore, various temperature measurements were conducted. Near the outer surfaces of the heating tube, temperatures were continuously measured using type C thermocouples at three fixed positions. Moreover, single temperature measurements were performed using a type B thermocouple at the outer surface of the reaction tube and the dosing tube. Finally, in the absence of the fuel stream and the carrier gas stream, temperatures inside the reactor were determined by introducing a type B thermocouple through the dosing tube inlet into the reactor [26]. The latter measurements were previously used for the calibration of the three heating zones and the design of experiments [15]. However, the previous calibration approach led to strong non-isothermal gas flows with strongly changing axial gas velocities in the second heating zone. Therefore, in this study, the experiments were designed using CFD simulations (see Section 2.7.1) and using simultaneous changes of both the carrier gas stream and

Table 1
Conditions of the DTR experiments: the operating temperatures T_{op}, the operating residence times $t_{res,op}$, the operating mass flow rates of the primary wood char $\dot{m}_{pwc,op}$, the operating gas volume flow rates (STP) of the carrier gas stream $\dot{V}_{cg,op,STP}$ and the operating gas volume flow rates (STP) of the secondary gas stream $\dot{V}_{sg,op,STP}$.

Experiment	T_{op} / K	$t_{res,op}$ / ms	$\dot{m}_{pwc,op}$ / g/min	$\dot{V}_{cg,op,STP}$ / l/min	$\dot{V}_{sg,op,STP}$ / l/min
P1000-200-MS	1273	200	1.517	0.76	17.44
P1100-200-MS	1373	200	1.450	0.70	16.17
P1200-200-MS	1473	200	1.197	0.66	15.07
P1300-200-MS	1573	200	1.182	0.61	14.11
P1400-200-MS	1673	200	1.225	0.58	13.27
P1600-200-MS	1873	200	1.023	0.52	11.85
P1000-400-MS	1273	400	0.758	0.38	8.72
P1200-400-MS	1473	400	0.554	0.33	7.54
P1400-400-MS	1673	400	0.555	0.29	6.64
P1600-400-MS	1873	400	0.401	0.26	5.93

the secondary gas stream to provide more homogeneous gas velocity and gas temperature conditions inside the drop-tube reactor. The experimental settings are summarised in Table 1. The experiments accordingly targeted operating temperatures T_{op} between 1273 K and 1873 K [26] and operating residence times $t_{res,op}$ of 200 ms [26] and 400 ms, each for the second heating zone. The experiments were carried out in a two-stage approach. Firstly, the experiments were performed without supplying wood char particles to determine the dry gas species concentrations at the outlet under inert conditions and to test the set flow rates of both the carrier gas stream and the secondary gas stream, as both flow rates strongly affect the balancing data (through the gas species concentration of argon at outlet, see Eq. (14)). Secondly, wood char particles were fed to the carrier gas steam to carry out the actual devolatilisation experiments.

During the experiments, the mass flow rates of the primary wood char $\dot{m}_{pwc}$, the gas volume flow rates (STP) of the carrier gas stream $\dot{V}_{cg,STP}$ and the gas volume flow rates (STP) of the secondary gas stream $\dot{V}_{sg,STP}$ were continuously recorded, while gas samples for the dry gas species concentrations measurements were taken about every 2 min. After the experimental campaign, periods of approximately 30 min with stationary conditions were defined for both the flow experiments without particles and the devolatilisation experiments with particles. Averages and corrected sample standard deviations of the recorded quantities were determined for each period. The standard deviations were usually small. However, the accuracy of the gas mass flow controller of the carrier gas stream was not sufficient for the experiments with operating residence times of 400 ms when the mass flow rate of the carrier gas stream was below 0.5 l/min (STP). In order not to affect the calculation of the balanced devolatilisation conversion $X_{dev,bal}$ (see Eq. (15)), the gas volume flow rate (STP) of the carrier gas stream $\dot{V}_{cg,STP}$ was determined by

$$\dot{V}_{cg,STP} = \dot{V}_{gas,in,STP} - \dot{V}_{sg,STP}\,, \tag{12}$$

where $\dot{V}_{gas,in,STP}$ is the gas volume flow rate (STP) at inlet and $\dot{V}_{sg,STP}$ is the gas volume flow rate (STP) of the secondary gas stream. The gas volume flow rate (STP) of the secondary gas stream $\dot{V}_{sg,STP}$ was obtained from the measurement data, while the gas volume flow rate (STP) at inlet $\dot{V}_{gas,in,STP}$ was calculated by

$$\dot{V}_{gas,in,STP} = \frac{\dot{V}_{sg,STP}}{r_{N_2,dry\ gas,out,0}}\,, \tag{13}$$

where $r_{N_2,dry\ gas,out,0}$ is the initial dry gas volume fraction of nitrogen at outlet. Similarly, the dry gas volume flow rate (STP) at outlet $\dot{V}_{dry\ gas,out,STP}$ was determined by

$$\dot{V}_{dry\ gas,out,STP} = \frac{\dot{V}_{cg,STP}}{r_{Ar,dry\ gas,out}}\,, \tag{14}$$

where $r_{Ar,dry\ gas,out}$ is the dry gas volume fraction of argon at outlet. Finally, the balanced devolatilisation conversion $X_{dev,bal}$ was calculated as the ratio of carbon detected in the gas to carbon fed as solid by

$$X_{dev,bal} = \frac{\dot{m}_{C,dry\ gas,out}}{w_{C,vol,0}\, w_{vol,pwc,0}\, \dot{m}_{pwc}}\,, \tag{15}$$

where

$$\dot{m}_{C,dry\ gas,out} = \sum_{i=CH_4,CO,CO_2} M_C\, r_{i,dry\ gas,out}\, \frac{p_{STP}\, \dot{V}_{dry\ gas,out,STP}}{\overline{R}\, T_{STP}} \tag{16}$$

is the carbon mass flow rate in the dry gas at outlet, $w_{C,vol,0}$ is the initial mass fraction of carbon in the volatiles of the dried primary wood char and $w_{vol,pwc,0}$ is the initial mass fraction of the volatiles in the dried primary wood char. Moreover, M_C is the molar mass of carbon, $r_{i,dry\ gas,out}$ is the volume fraction of species i in the dry gas at outlet, $p_{STP} = 1.01325$ bar is the standard pressure (STP), $\overline{R}$ is the molar gas constant and $T_{STP} = 273.15$ K is the standard temperature (STP). The initial mass fraction of the volatiles in the dried primary wood char $w_{vol,part,0}$ and the initial mass fraction of carbon in the volatiles of the dried primary wood char $w_{C,vol,0}$ were obtained from the equilibrium results (see Section 2.2). Specifically, (i) the equilibrium-derived volatiles mass fraction of the sieved primary char (batch DTR) on dry basis was used as mass fraction $w_{vol,pwc,0}$ and (ii) the equilibrium-derived mass fraction of carbon in the volatiles of the sieved primary char (batch DTR) on dry basis was applied as mass fraction $w_{C,vol,0}$.

2.6. TG kinetics

TG kinetics were derived from the experimental TG and DTG curves using distributed activation energy models [39–41]. Such models are considered as appropriate for the extrapolation to high heating rates (for example, see [42]) and can be derived using distribution-free methods [42,43] or distribution-fitting methods. The latter methods are typically combined with single first-order reaction Gauss distributed activation energy models but have also been coupled with multi-reaction Gauss distributed activation energy models as well as analogous models based on double-Gauss, Weibull or logistic distributions (see [39]).

In this study, the TG analyses were performed at approximately constant heating rates. Therefore, the heating rates were assumed to be constant for the regression. The temperature T during the heat-up was calculated by

$$T = \begin{cases} T_0 + \beta\, t\,, & \text{if} \quad 0 < t < \dfrac{T_{max} - T_0}{\beta} \\ T_{max}\,, & \text{if} \quad t > \dfrac{T_{max} - T_0}{\beta} \end{cases}\,, \tag{17}$$

where T_0 is the initial temperature, β is the (constant) heating rate, t is the time and T_{max} is the maximum temperature.

Assuming pseudo-species and parallel reactions, the calculated mass fraction of the remaining volatiles $w_{rv,calc}$, the time derivative of the calculated mass fraction of the remaining volatiles $\mathrm{d}w_{rv,calc}/\mathrm{d}t$ and the temperature derivative of the calculated mass fraction of the remaining volatiles $\mathrm{d}w_{rv,calc}/\mathrm{d}T$ were determined by

$$w_{rv,calc} = 1 - \sum_{i=1}^{N} w_{rv,calc,i,0} + \sum_{i=1}^{N} w_{rv,calc,i}\,, \tag{18}$$

$$\frac{\mathrm{d}w_{rv,calc}}{\mathrm{d}t} = \sum_{i=1}^{N} \frac{\mathrm{d}w_{rv,calc,i}}{\mathrm{d}t}\,, \tag{19}$$

$$\frac{\mathrm{d}w_{rv,calc}}{\mathrm{d}T} = \sum_{i=1}^{N} \frac{\mathrm{d}w_{rv,calc,i}}{\mathrm{d}T}\,, \tag{20}$$

where N is the number of parallel reactions, $w_{rv,calc,i}$ is the calculated mass fraction of the remaining volatiles for reaction i and $w_{rv,calc,i,0}$ is the initial calculated mass fraction of the remaining volatiles for reaction i. The latter is defined by

$$w_{rv,calc,i,0} = w_{rv,calc,i}\Big|_{t=0} = w_{rv,calc,i}\Big|_{T=T_0}\,, \tag{21}$$

while the calculated mass fraction of the remaining volatiles $w_{\mathrm{rv,calc},i}$, the time derivative of the calculated mass fraction of the remaining volatiles $\mathrm{d}w_{\mathrm{rv,calc},i}/\mathrm{d}t$ and the temperature derivative of the calculated mass fraction of the remaining volatiles $\mathrm{d}w_{\mathrm{rv,calc},i}/\mathrm{d}T$ were calculated according to [39] by

$$w_{\mathrm{rv,calc},i} = \int_0^\infty \exp\left(- \int_{T_0}^{T} \frac{k_i\left(\overline{E}_\mathrm{a}, \widetilde{T}\right)}{\beta} \mathrm{d}\widetilde{T} \right) f_i\left(\overline{E}_\mathrm{a}\right) \mathrm{d}\overline{E}_\mathrm{a}\,, \tag{22}$$

$$\frac{\mathrm{d}w_{\mathrm{rv,calc},i}}{\mathrm{d}t} = \beta \frac{\mathrm{d}w_{\mathrm{rv,calc},i}}{\mathrm{d}T}\,, \tag{23}$$

$$\frac{\mathrm{d}w_{\mathrm{rv,calc},i}}{\mathrm{d}T} = \int_0^\infty \frac{k_i\left(\overline{E}_\mathrm{a}, T\right)}{\beta} \exp\left(- \int_{T_0}^{T} \frac{k_i\left(\overline{E}_\mathrm{a}, \widetilde{T}\right)}{\beta} \mathrm{d}\widetilde{T} \right) f_i\left(\overline{E}_\mathrm{a}\right) \mathrm{d}\overline{E}_\mathrm{a}\,, \tag{24}$$

where k_i is the rate constant and f_i is the probability density function, each of reaction i. The former is given by

$$k_i\left(\overline{E}_\mathrm{a}, T\right) = k_{0,i} \exp\left(-\frac{\overline{E}_{\mathrm{a},i}}{\overline{R}\,T} \right), \tag{25}$$

where $k_{0,i}$ is the pre-exponential factor of reaction i, $\overline{E}_{\mathrm{a},i}$ is the molar activation energy of reaction i and $\overline{R}$ is the molar gas constant.

Preliminary tests showed that four first-order reactions and logistic distributions are most appropriate for the regression in the course of this study. Therefore, the probability density function of reaction i f_i is described by

$$f_i\left(\overline{E}_\mathrm{a}\right) = \frac{1}{s} \frac{\exp(-y)}{(1+\exp(-y))^2} \tag{26}$$

where

$$y = \frac{\overline{E}_\mathrm{a} - \mu_{\overline{E}_\mathrm{a},i}}{\sqrt{3}/\pi\, \sigma_{\overline{E}_\mathrm{a},i}}\,,$$

$$s = \sqrt{3}/\pi\, \sigma_{\overline{E}_\mathrm{a},i}\,.$$

$\mu_{\overline{E}_\mathrm{a},i}$ and $\sigma_{\overline{E}_\mathrm{a},i}$ are the expectation and the standard deviation of the logistic distribution for the molar activation energy $\overline{E}_\mathrm{a}$ and the reaction i.

In order to determine approximations for the pre-exponential factors $\boldsymbol{k}_0 = (k_{0,i})$, the expectations $\boldsymbol{\mu}_{\overline{E}_\mathrm{a}} = \left(\mu_{\overline{E}_\mathrm{a},i}\right)$, the standard deviations $\boldsymbol{\sigma}_{\overline{E}_\mathrm{a}} = \left(\sigma_{\overline{E}_\mathrm{a},i}\right)$ and the initial calculated mass fractions of the remaining volatiles $\boldsymbol{w}_{\mathrm{rv,calc},0} = \left(w_{\mathrm{rv,calc},i,0}\right)$, regressions were performed using Eqs. (18)–(26) and the *trapz*, *quadgk*, *fminsearch* and *fmincon SPQ* methods of Matlab [38]. The *trapz* (trapezoidal quadrature) method with 60 equally spaced intervals and the *quadgk* (Gauss-Konrad quadrature) method were applied to the outer integrals and the inner integrals, respectively. The percentiles at 0.0001 and 0.9999 of the logistic distributions were used as limits of the outer integrals. The *fminsearch* was used to obtain appropriate initial parameters for the final optimisation using the *fmincon SPQ* method. In the final optimisation, constraints were applied to ensure that the calculated mass fraction of the remaining volatiles $w_{\mathrm{rv,calc}}$ is appropriately described for $T \to \infty$, i. e. $w_{\mathrm{rv,calc}} \to 0$.

2.7. DTR kinetics

DTR kinetics were obtained using several iterations of sequential CFD simulations and numerical optimisations. The CFD simulations provided profiles of the axial gas velocity, the axial gas temperature and the axial gas species concentrations as input for the numerical optimisation. The first CFD simulations were performed with appropriate initial guesses for the kinetic parameters, whereas the subsequent CFD simulations were carried out using improved kinetic parameters obtained in the preceding numerical optimisation. The CFD simulations are focussed in Section 2.7.1 while the numerical optimisation methods are presented in Section 2.7.2.

2.7.1. CFD simulations

The CFD simulations of the DTR experiments were carried out using the CFD model described in Section S3. The model pays specific attention to the wall temperatures, the particle injections and the particle devolatilisation rates.

The wall temperatures are described using approximations based on sigmoid functions. The approximations were obtained using the measured temperatures and least-squares regressions and are shown as solid continuous lines in Figs. S1–S10.

The particle injections are defined (i) using the gas condition of the carrier gas stream, (ii) using the measured particle size distribution of the sieved wood char batch (see Sections 2.3 and 3.2) and (iii) assuming spherical particle shapes and an uniform mass flux distribution.

The particle devolatilisation rates are described by either a single first-order reaction Arrhenius law model (SFORALM) with two model parameters or a modified Yamamoto model (MYM) [44,45] with five model parameters, i. e. with an increased number of model parameters in comparison with the single first-order reaction Arrhenius law model. The reaction rate of the single first-order reaction Arrhenius law model R_{SFORALM} and the reaction rate of the modified Yamamoto model R_{MYM} are given by

$$R_{\mathrm{SFORALM}} = k_0 \exp\left(-\frac{\overline{E}_\mathrm{a}}{\overline{R}\,T_\mathrm{part}} \right) \left(m_\mathrm{part} - m_{\mathrm{part,min,dev}}\right), \tag{27}$$

$$R_{\mathrm{MYM}} = F\, k_0 \exp\left(-\frac{\overline{E}_\mathrm{a}}{\overline{R}\,T_\mathrm{part}} \right) \left(m_\mathrm{part} - m_{\mathrm{part,min,dev}}\right), \tag{28}$$

where k_0 is the pre-exponential factor, $\overline{E}_\mathrm{a}$ is the molar activation energy, $\overline{R}$ is the molar gas constant, T_part is the particle temperature, m_part is the particle mass, $m_{\mathrm{part,min,dev}} = \left(1 - w_{\mathrm{vol,part},0}\right) m_{\mathrm{part},0}$ is the particle mass after complete devolatilisation, $w_{\mathrm{vol,part},0}$ is the initial volatiles mass fraction of the particle, $m_{\mathrm{part},0}$ is the initial particle mass and F is a modification factor. The factor F was introduced to describe the pre-exponential factor as function of the devolatilisation conversion X_dev without significantly increasing the computing time [44] and was slightly adapted in this study through replacing the polynomial of fourth order by a polynomial of second order. The factor F used in this study is given by

$$F = \sum_{i=1}^{3} C_i\, X_\mathrm{dev}^{i-1}\,, \tag{29}$$

where C_1, C_2 and C_3 are coefficients. The devolatilisation conversion X_dev is defined by

$$X_\mathrm{dev} = \frac{m_{\mathrm{part},0} - m_\mathrm{part}}{m_{\mathrm{part},0} - m_{\mathrm{part,min,dev}}}\,. \tag{30}$$

The model in particular assumes that the particles are isothermal, have equivalent diameters and do not show fragmentation. These assumptions are strong simplifications considering the observed particle sizes and particles shapes (see Section 3.2) and previous findings for the effects of particle shapes [19] and uncorrected kinetics [21]. However, in the absence of sufficiently detailed experimental data of particle morphology, particle break-up, particle thermal conductivity and particle velocity for model development and validation, the simplified approach is considered as a good compromise between model complexity, computational requirements and applicability for design and scale-up. Furthermore, the wood char particles applied in the DTR experiments have mainly equivalent diameters below 100 µm, in particular after fragmentation, and likely higher aspect ratios in the case of particles above 150 µm (see Section 3.2). Not only the small but most of the particles should therefore satisfy the common criterion $Bi \ll 1$ assuming

effective particle thermal conductivities of 0.1–0.2 W/(m K) [21,46]. In summary, the isothermal approach is justified as a first approximation. Future studies may increase the model complexity using additional data to derive improved kinetics. Such studies may also increase the extent of validation. As the reactor has small dimensions and limited access possibilities, only temperature measurements could be carried out to generate validation data (see Sections 2.5 and 3.5), while measurements of axial gas velocities, axial particle velocities, axial gas species concentrations were impeded in this study. However, it is expected that the gas phase modelling provides reasonable predictions due to the laminar flow and the calibrated wall boundary conditions while the particle modelling could have larger uncertainties due to the impact of particle morphology on particle flow and particle heat and mass transfer.

2.7.2. Numerical optimisation methods

The numerical optimisations were conducted using an in-house software that uses the profiles of the axial gas velocity, the axial gas temperature and the axial gas species concentrations as input and performs zero-dimensional single-particle simulations similar to the particle tracking simulations in the CFD simulations. The initial particle properties are defined using the measured particle size distributions, while the particle equations are subsequently integrated using the LSODA (Adams/BDF) method [47,48], that is implemented in the *solve_ivp* method of SciPy [49,50]. The simulated devolatilisation conversion $X_{\mathrm{dev,sim}}$ is defined by

$$X_{\mathrm{dev,sim}} = \frac{\dot{m}_{\mathrm{part},0} - \sum_i \dot{N}_{\mathrm{part},i}\, m_{\mathrm{part},i}}{\dot{m}_{\mathrm{part},0} - \left(1 - w_{\mathrm{vol,part},0}\right)\, \dot{m}_{\mathrm{part},0}}\,, \tag{31}$$

where $\dot{m}_{\mathrm{part},0}$ is the initial particle mass flow rate, $\dot{N}_{\mathrm{part},i}$ is the particle number flow rate with respect to particle injection i and $m_{\mathrm{part},i}$ is the particle mass with respect to particle injection i. The particle number flow rate with respect to particle injection i $\dot{N}_{\mathrm{part},i}$ is given by

$$\dot{N}_{\mathrm{part},i} = \frac{\dot{m}_{\mathrm{part},0,i}}{m_{\mathrm{part},0,i}} = \frac{\dot{m}_{\mathrm{part},0,i}}{\rho_{\mathrm{part}}\, \frac{\pi}{6}\, d^3_{\mathrm{part},0,i}}\,, \tag{32}$$

where $m_{\mathrm{part},0,i}$ is the initial particle mass with respect to particle injection i, ρ_{part} is the particle density and $d_{\mathrm{part},0,i}$ is the initial particle diameter with respect to particle injection i.

For the optimisation of the devolatilisation kinetic parameters using the *least_squares* method of SciPy [49,50], the residual R was defined using the simulated devolatilisation conversions $X_{\mathrm{dev,sim}}$ and the balanced devolatilisation conversions $X_{\mathrm{dev,bal}}$ of all DTR experiments. The residual R is given by

$$R = \sum_{j \in J} X_{\mathrm{dev,bal},j} - X_{\mathrm{dev,sim},j}\,, \tag{33}$$

where J is the set of all DTR experiments.

3. Results

This section presents (i) the results of the chemical analyses, the particle size distribution measurements, the TG analyses and the DTR experiments and (ii) the derived TG and DTR kinetics.

3.1. Chemical analyses

Elemental and proximate compositions of the sieved and the unsieved wood-chars are summarised in Tables S3 and S4, while lower heating values (LHV) and higher heating values (HHV) of the unsieved and the sieved wood-chars, that were used to derive the devolatilisation enthalpy complying with the energy balance (see [5]), are given in Table S5. Slight deviations in the carbon, hydrogen, oxygen and nitrogen contents of the sieved and the unsieved wood-chars are most likely due to sieving, sampling and the analysis methods and need to be accepted. The deviations in the water contents can be attributed to different humidities, while the deviations in the measured fixed carbon and volatiles contents could be caused by the fuel variability and the analysis methods. However, measured water contents were only determined for the sake of completeness, as dried samples were applied in both DTR experiments and TG analyses. Furthermore, measured fixed carbon and volatiles contents were not used for subsequent calculations, as some volatiles are typically not released during the analyses due to too low temperatures and too short residence times (see Tables S3 and S4). Instead, equilibrium-derived fixed carbon and volatiles contents (see Section 2.2) were applied in this study. These contents are given in Table S6 and enable a consistent mathematical description of the particle composition during devolatilisation and heterogeneous gasification (see [5]). The equilibrium-derived devolatilisation conversions based on carbon balancing $X_{\mathrm{dev,eqd,C}}$, based on hydrogen balancing $X_{\mathrm{dev,eqd,H}}$ and based on oxygen balancing $X_{\mathrm{dev,eqd,O}}$ and the mean equilibrium-derived devolatilisation conversions $X_{\mathrm{dev,eqd}}$ are given in Table 2. Accordingly, the deviations between the equilibrium-derived devolatilisation conversions $X_{\mathrm{dev,eqd,C}}$, $X_{\mathrm{dev,eqd,H}}$ and $X_{\mathrm{dev,eqd,O}}$ are mainly low which justifies simple arithmetic averaging.

Table 2
Equilibrium-derived devolatilisation conversions based on carbon balancing $X_{\mathrm{dev,eqd,C}}$, based on hydrogen balancing $X_{\mathrm{dev,eqd,H}}$ and based on oxygen balancing $X_{\mathrm{dev,eqd,O}}$ and mean equilibrium-derived devolatilisation conversions $X_{\mathrm{dev,eqd}}$ of the samples collected in the DTR experiments.

Sample	$X_{\mathrm{dev,eqd,C}}$	$X_{\mathrm{dev,eqd,H}}$	$X_{\mathrm{dev,eqd,O}}$	$X_{\mathrm{dev,eqd}}$
Secondary char, P1000-200-MS	0.44	0.49	0.45	0.46
Secondary char, P1100-200-MS	0.69	0.72	0.72	0.71
Secondary char, P1200-200-MS	0.65	0.86	0.62	0.71
Secondary char, P1300-200-MS	0.72	0.90	0.69	0.77
Secondary char, P1400-200-MS	0.80	0.93	0.80	0.84
Secondary char, P1600-200-MS	0.97	0.93	0.97	0.96
Secondary char, P1000-400-MS	0.64	0.64	0.65	0.64
Secondary char, P1200-400-MS	0.73	0.90	0.71	0.78
Secondary char, P1400-400-MS	0.81	0.93	0.82	0.85
Secondary char, P1600-400-MS	0.94	0.93	0.93	0.93

3.2. Particle size distribution measurements

The particle size distributions of the unsieved primary wood char and the sieved primary wood char are shown in Fig. 2. Thus, the particle size distribution of the sample material strongly changed during sieving (50–150 µm). Firstly, approximately 75% and 2.5% of the original sample material were below 50 µm and above 150 µm, respectively. Thus, approximately 27.5% of the original sample material only was retrieved in the sieved sample material. Secondly, particles larger than 50 µm accounted for more than 76% after sieving compared to 25% before sieving. Thus, sieving successfully reduced the small fractions. Thirdly, approximately 23% of the sieved sample material is smaller than 50 µm, as wood char particles are porous and fragile when exposed to mechanical stress (see Figs. S11–S15). Fourthly, approximately 11% of the sieved sample material is larger than 150 µm, as (i) the particle shapes (elongated to nearly cubic, see also Fig. S11) affected the fractionation by sieving and (ii) the particle size measurements were affected by the alignment of the particles relative to the laser beam (as laser diffraction provides equivalent diameters). Furthermore, the particle size distribution of the particles extracted in the DTR experiment P1400-200-MS is shown in Fig. 2. This distribution matches the distribution of the primary unsieved wood char by coincidence and demonstrates significant particle size changes in the DTR experiment. The particles most likely experienced fragmentation and broke up at inner positions.

3.3. TG analyses

The averaged experimental TG curves are shown in Fig. 3. Firstly, the curves demonstrate that the TG data for 5 K/min overlaps the

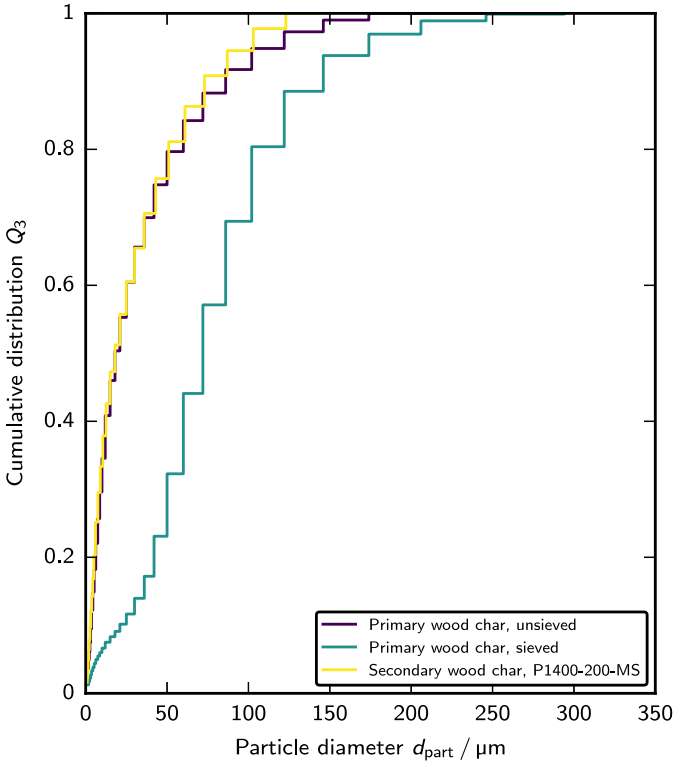

Fig. 2. Particle size distributions of the unsieved primary wood char, the sieved primary wood char and the secondary wood char obtained in the DTR experiment P1400-200-MS.

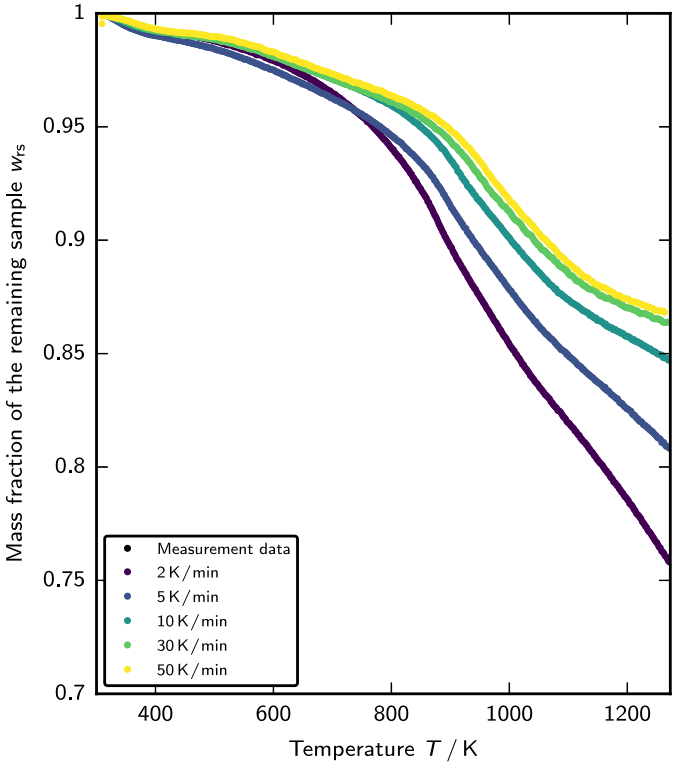

Fig. 3. TG curves: measurement data as function of temperature for various heating rates.

other data between 300 K and 800 K. Despite good repeatability, fuel property fluctuations caused by the small sample material could have strongly affected the TG analyses at this heating rate. Therefore, the TG data for 5 K/min was discarded for the subsequent approximations. Secondly, the curves show (i) that the mass decrease mainly occurs above 800 K, (ii) that the remaining sample mass at the maximum temperature decreases with decreasing heating rate and (iii) that the remaining sample masses at the maximum temperature for heating rates of 2 K/min and 5 K/min were below the masses that are expected corresponding to the equilibrium calculations (see Sections 2.2 and 3.1). Furthermore, experimental TG curves of long-term analyses at 1273 K after heating-up with 50 K/min shown in Fig. S24 demonstrate a continuing mass decrease for more than 1100 min. The remaining sample mass after 1440 min was approximately 7% of the initial sample mass and thus well below the mass expected corresponding to the equilibrium calculations. Thus, devolatilisation was interfered by combustion due to the presence of oxygen. However, recalling that typical conversion times are less than 10 min at 21273 Pa O_2 and 1123 K and approximately 100 min at 5065 Pa O_2 and 673 K [51], only tiny partial pressures of oxygen are expected. Specifically, for a measured mean reaction rate of $1.5 \cdot 10^{-5}\ s^{-1}$ at a temperature of 1273 K (see Fig. S25), available kinetics [52] (derived for 2.25%-36% O_2 and 573-773 K) provide rough estimates for the partial pressure of oxygen well below 1 Pa. Furthermore, the impact was likely larger for 2 K/min and 5 K/min than for 30 K/min and 50 K/min due to the longer analysis times. Moreover, the release of the volatiles could have mainly impeded oxygen adsorption during the main devolatilisation stages. Therefore, the averaged TG curves (reflecting the measured mass fraction of the remaining sample $w_{rs,meas}$) were modified using the cut-off approach (see Sections 2.4 and S4). The modified TG curves (providing the measured mass fraction of the remaining volatiles $w_{rv,meas}$) for 2 K/min, 5 K/min, 30 K/min and 50 K/min are depicted in Fig. 4 (left), while the corresponding DTG curves are shown in Fig. 4 (right). All DTG curves are characterised by strong peaks below 400 K and between 900 K and 1000 K. In addition, rather flat peaks of the DTG curves are observed between 500 K and 800 K for 30 K/min and 50 K/min. The gas release below 400 K and the corresponding peaks can be explained by the release of enclosed humidity in the inner pores of the sample material. The comparability of TG and DTR kinetics, however, should not be affected as the same drying procedures were applied for both the TG analyses and the DTR experiments.

3.4. TG kinetics

The results of the numerical optimisation, that relied on the experimental results for 2 K/min, 5 K/min, 30 K/min and 50 K/min only, are shown in Fig. 4. Accordingly, the calculated TG and DTG curves based on multi first-order reaction logistic distributed activation energy models provide good estimates for the conversion. The parameters of the curves are given in Table 3.

3.5. DTR experiments

The measured N_2-Ar free and dry gas species mole fractions $\boldsymbol{x}_{N_2\text{-Ar free and dry gas,out}} = \left(x_{i,N_2\text{-Ar free and dry gas,out}}\right)$ are shown in Fig. 5 and are given in Table S7. Furthermore, the volatiles mole fractions at atmospheric conditions based on equilibrium calculations (see Section 2.2) are shown for comparison in Fig. 6. In this context, it should be emphasised that the equilibrium amounts do not reflect typical non-equilibrium observations and are strongly affected by the water-gas shift equilibrium, leading to high contents of water and methane at equilibrium temperatures below 1000 K and tiny contents at equilibrium temperatures above 1200 K. In contrast, significant mole fractions of CH_4 were detected for the DTR experiments P1000-200-MS and P1200-200-MS. The mole fractions of H_2 (mainly between 0.708 and 0.735), however, are in agreement with the equilibrium mole

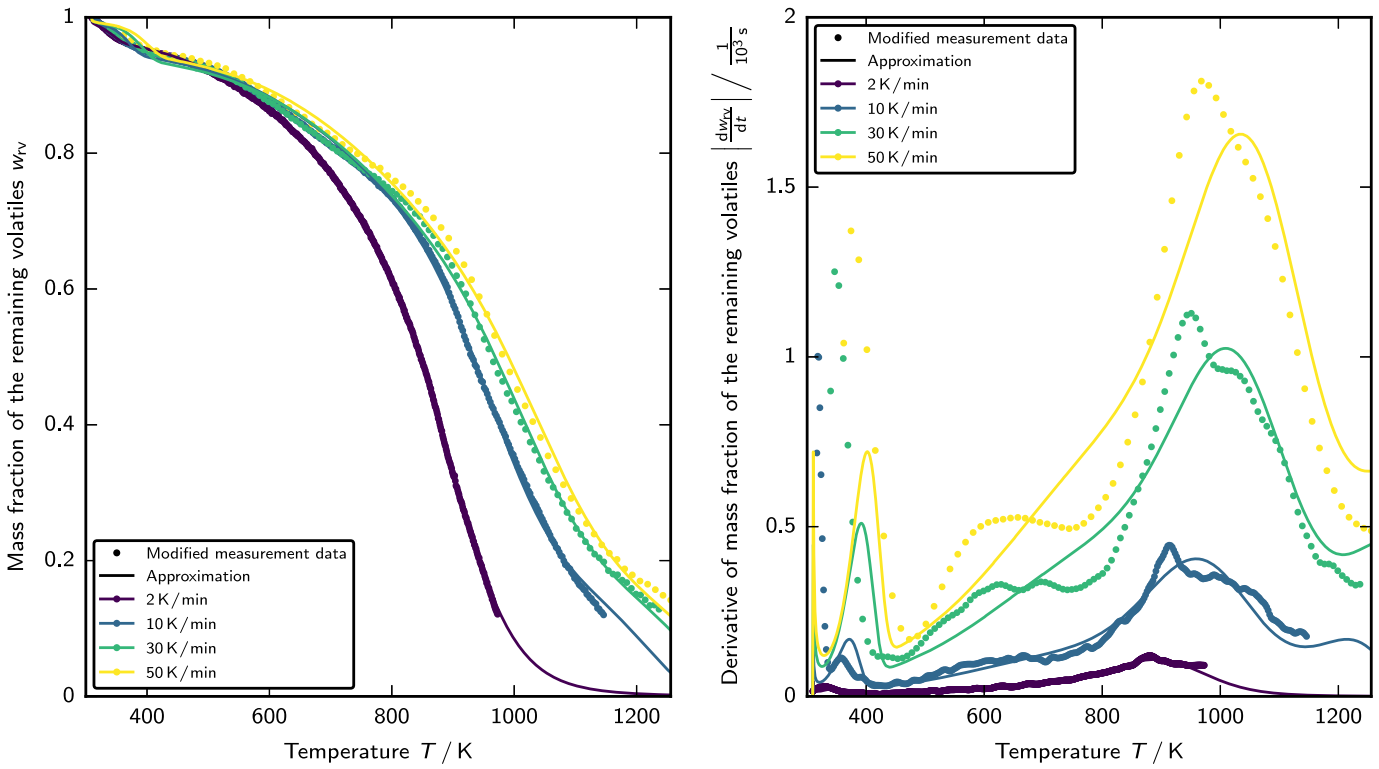

Fig. 4. TG curves (left) and DTG curves (right): modified measurement data and approximations based on the multi first-order reaction logistic distributed activation energy model, each as function of temperature for various heating rates.

Table 3
Parameters for the calculation of the mass fraction of the remaining volatiles w_{rv} and the derivative of the mass fraction of the remaining volatiles dw_{rv}/dt based on the multi first-order reaction logistic distributed activation energy model using Eqs. (18)-(26).

i	$\frac{k_{0,i}}{1/s}$	$\frac{\mu_{\overline{E}_a,i}}{J/mol}$	$\frac{\sigma_{\overline{E}_a,i}}{J/mol}$	$w_{rv,calc,i,0}$			
				$2\,\frac{K}{min}$	$10\,\frac{K}{min}$	$30\,\frac{K}{min}$	$50\,\frac{K}{min}$
1	$2.038 \cdot 10^6$	$5.950 \cdot 10^4$	$1.070 \cdot 10^1$	$2.129 \cdot 10^{-2}$	$4.242 \cdot 10^{-2}$	$4.746 \cdot 10^{-2}$	$4.128 \cdot 10^{-2}$
2	$4.727 \cdot 10^3$	$9.179 \cdot 10^4$	$2.704 \cdot 10^4$	$3.750 \cdot 10^{-1}$	$3.425 \cdot 10^{-1}$	$4.246 \cdot 10^{-1}$	$4.530 \cdot 10^{-1}$
3	$7.916 \cdot 10^5$	$1.985 \cdot 10^5$	$6.838 \cdot 10^2$	0	$1.377 \cdot 10^{-1}$	$1.340 \cdot 10^{-1}$	$1.224 \cdot 10^{-1}$
4	$2.789 \cdot 10^5$	$1.495 \cdot 10^5$	$1.310 \cdot 10^4$	$6.037 \cdot 10^{-1}$	$4.773 \cdot 10^{-1}$	$3.939 \cdot 10^{-1}$	$3.833 \cdot 10^{-1}$

fractions of H_2 above temperatures of 1273 K (approximately between 0.703 and 0.710). Furthermore, the mole fraction of CO_2 (up to 0.082) decreases with increasing operating temperature and increasing operating residence time for the second heating zone, while the mole fraction of CO (between 0.214 and 0.290) increases with both operating parameters. The findings are to be expected as the gas species concentrations at outlet shift towards equilibrium with increasing operating temperature and increasing operating residence time.

The measured gas temperatures are compared with the CFD predicted gas and particle temperatures in Figs. 7–8 and S16–S23. The predicted gas temperatures are accordingly in good agreement with the measured data for the first two heating zones as, in particular, the axial gas temperature decrease at the end of the dosing tube is clearly reflected. In contrast, large deviations can be found for the third heating zone, most likely due to the uncertainties in the axial positioning of the thermocouple. The particle temperatures are shown for particles close to the reactor axis with particle diameters of 0.95 µm (bin 0), 55.77 µm (bin 20), 133.46 µm (bin 25) and 320.78 µm (bin 30). 0.95 µm and 320.78 µm are the minimum particle diameter and the maximum particle diameter of the injected particles. Small particles with diameters of up to 30-40 µm thus experience temperatures similar to the gas temperatures while particle temperatures of large particles strongly deviate from the predicted gas temperatures confirming the need of advanced approaches for the development of DTR kinetics.

The balanced devolatilisation conversions $X_{dev,bal}$ (see Eq. (15)) are given in Table 4 and are in agreement with the expected trends. The balanced devolatilisation conversion $X_{dev,bal}$ thus increases with increasing operating temperature and increasing operating residence time for the second heating zone. Furthermore, the balanced devolatilisation conversions $X_{dev,bal}$ are compared with the mean equilibrium-derived devolatilisation conversions $X_{dev,eqd}$ (see Eq. (9)) in Fig. 9 showing that the equilibrium-derived devolatilisation conversions $X_{dev,eqd}$ are significantly larger than the balanced devolatilisation conversions $X_{dev,bal}$. Following the preceding study [15], the balanced devolatilisation conversions $X_{dev,bal}$ were applied to derive the DTR kinetics as the gas species concentrations measurements are considered as more meaningful than the chemical analysis results.

The uncertainties due to the gas species concentrations measurements are reflected in Fig. 9. The uncertainty bars were defined using the Gaussian propagation of uncertainty for the balanced devolatilisation conversions. Thus, the balanced devolatilisation conversions for operating residence times of 400 ms are significantly stronger affected

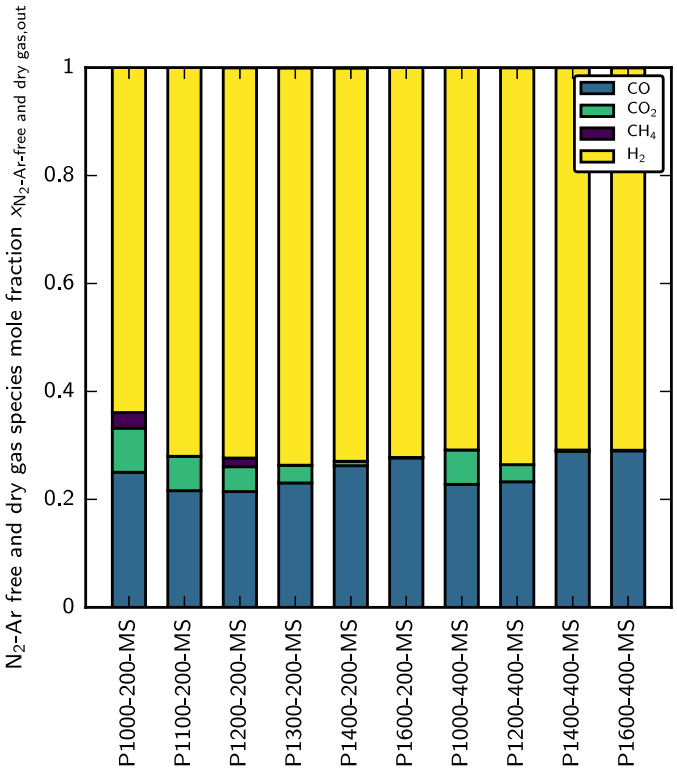

Fig. 5. Measured N_2-Ar-free and dry gas composition at the outlet in mole fractions.

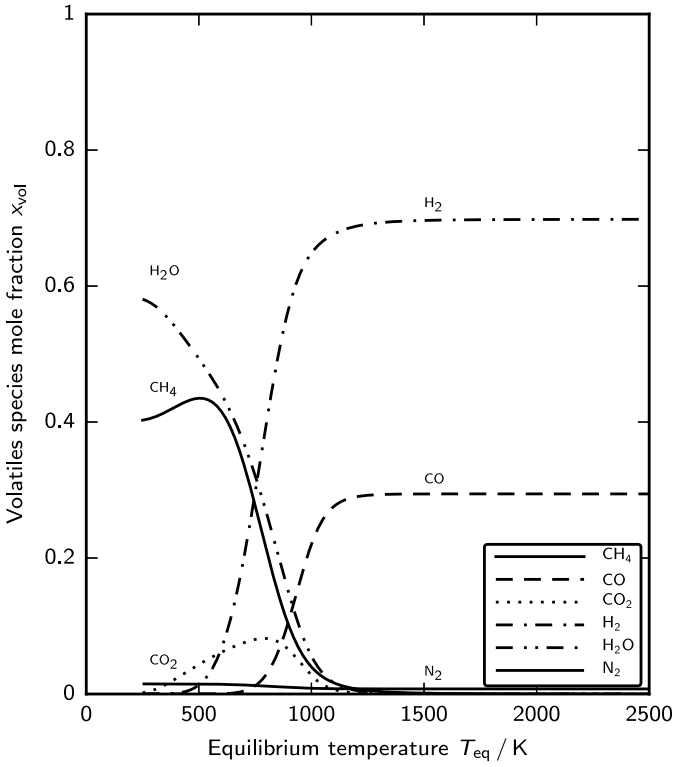

Fig. 6. Equilibrium volatiles composition at atmospheric conditions in mole fractions.

by uncertainties than balanced devolatilisation conversions for operating residence times of 200 ms. This demonstrates the challenges in this study to operate the mass flow controller of the carrier gas stream below 0.5 l/min (STP) (see Section 2.5).

Table 4
Balanced devolatilisation conversions $X_{dev,bal}$ of the DTR experiments.

Experiment	$X_{dev,bal}$
P1000-200-MS	0.41
P1100-200-MS	0.42
P1200-200-MS	0.54
P1300-200-MS	0.59
P1400-200-MS	0.68
P1600-200-MS	0.76
P1000-400-MS	0.41
P1200-400-MS	0.57
P1400-400-MS	0.84
P1600-400-MS	0.88

3.6. DTR kinetics

The results of the numerical optimisation are given in Table 5 and are demonstrated for the single first-order reaction Arrhenius law model (SFORALM) in Fig. 10 and for the modified Yamamoto model (MYM) in Fig. 11. The simulated devolatilisation conversions $X_{dev,sim}$ are accordingly in good agreement with the balanced devolatilisation conversions $X_{dev,bal}$ for both kinetics, while the modified Yamamoto model provides slightly superior results in comparison with the single first-order reaction Arrhenius law model. However, the accuracy of the kinetics is restricted by the targeted experiments, by the accuracy of the measured gas species concentrations and by the model assumptions:

1. Operating residence times of approximately 200 ms and 400 ms were used for the design of the experiments (see Section 2.5). Thus, the devolatilisation kinetics could provide significantly deviating predictions of the devolatilisation conversion X_{dev} outside this range.
2. The particle sizes were assumed to be constant in the single-particle simulations (see Section 2.7.1) as implementation of fragmentation is an elaborative venture. However, particle size changes, that typically accompany devolatilisation (for example, see [18,53]), were found for the DTR experiments (see Section 3.2). Therefore, numerical optimisation of the DTR kinetics based on the single first-order reaction Arrhenius law model was also performed using the particle size distributions of the particles obtained after the extraction (see Section 3.2). The optimisation results demonstrated that quite similar kinetic parameters can be obtained for the single first-order reaction Arrhenius law model while the simulated devolatilisation conversions in the DTR experiments increase approximately up to 10%. Therefore, it is expected that fragmentation has only a minor impact on the accuracy of the DTR kinetics.
3. The small dimensions of the dosing tube with an inner diameter of 4 mm challenged the axial dosing of the particles in the DTR experiments. Therefore, some particles likely moved in the wall boundary layer and experienced temperature histories and residence times that strongly deviate from the temperature histories and residence times of particles moving along the axis. Moreover, the dosing tube slightly bent during the DTR experiments, which likely caused particles to collide with the inner surface of the dosing tube. This probably led to abrasion and faster heat-up and consequently to intensified devolatilisation and fragmentation. Although uncertainty quantification is hardly possible, it is expected that the uncertainties of both impacts are similar to those estimated for fragmentation.

Finally, the simulated devolatilisation conversions at various distances from the dosing tube inlet are compared in Table 6. The devolatilisation conversions at the end of the first heating zone (the end of the dosing tube) are up to 40% and are higher for longer operating residence times and smaller particles. The devolatilisation

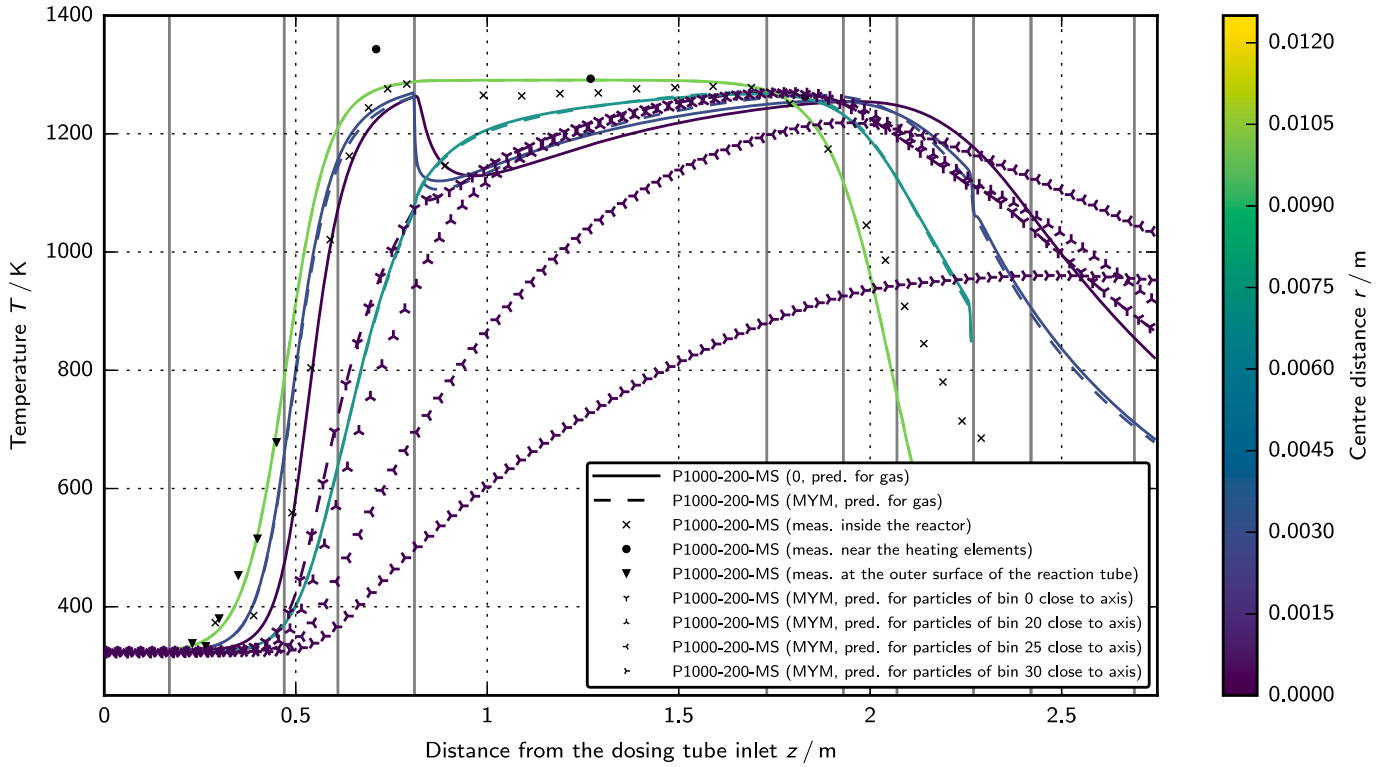

Fig. 7. Measured temperatures and predicted gas and particle temperatures for the DTR experiment P1000-200-MS. Measurements were performed using type B and type C thermocouples (see Section 2.5), while predictions were obtained for initial conditions without particles (0) and using the modified Yamamoto model (MYM). Predicted gas temperatures are shown for centre distances of 0 mm, 2.98 mm, 6.5 mm and 9.98 mm, while predicted particle temperatures are shown for particles close to the reactor axis with particle diameters of 0.95 µm (bin 0), 55.77 µm (bin 20), 133.46 µm (bin 25) and 320.78 µm (bin 30).

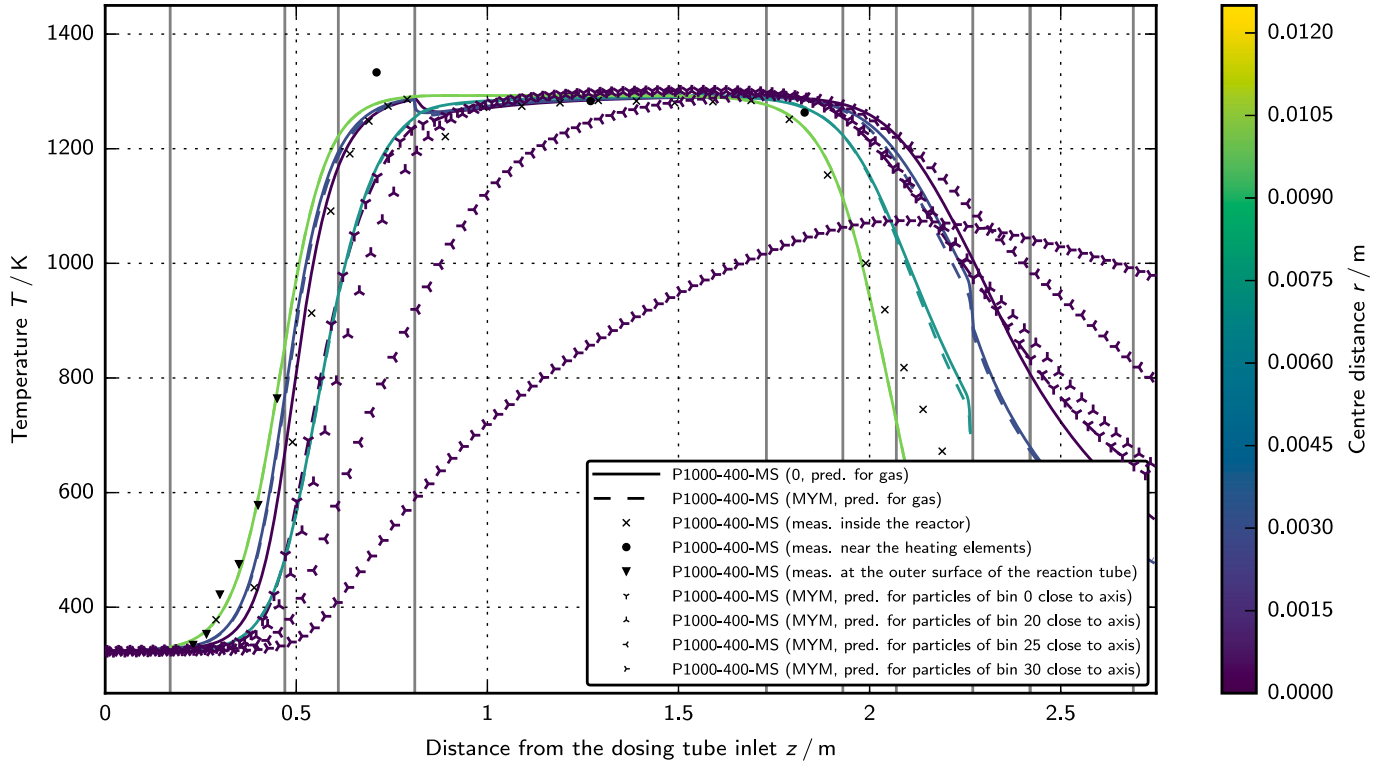

Fig. 8. Measured temperatures and predicted gas and particle temperatures for the DTR experiment P1000-400-MS. Measurements were performed using type B and type C thermocouples (see Section 2.5), while predictions were obtained for initial conditions without particles (0) and using the modified Yamamoto model (MYM). Predicted gas temperatures are shown for centre distances of 0 mm, 2.98 mm, 6.5 mm and 9.98 mm, while predicted particle temperatures are shown for particles close to the reactor axis with particle diameters of 0.95 µm (bin 0), 55.77 µm (bin 20), 133.46 µm (bin 25) and 320.78 µm (bin 30).

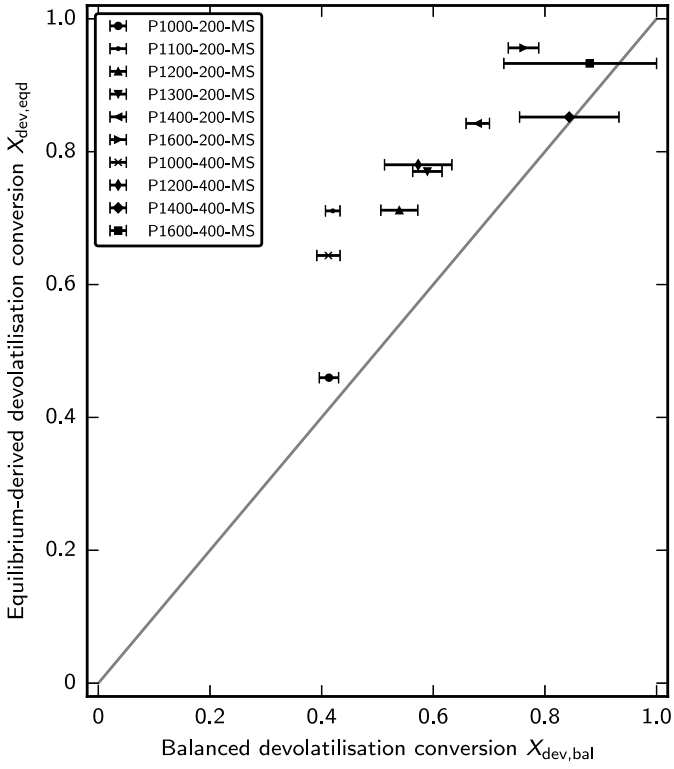

Fig. 9. Mean equilibrium-derived devolatilisation conversions $X_{dev,eqd}$ in comparison with balanced devolatilisation conversions $X_{dev,bal}$.

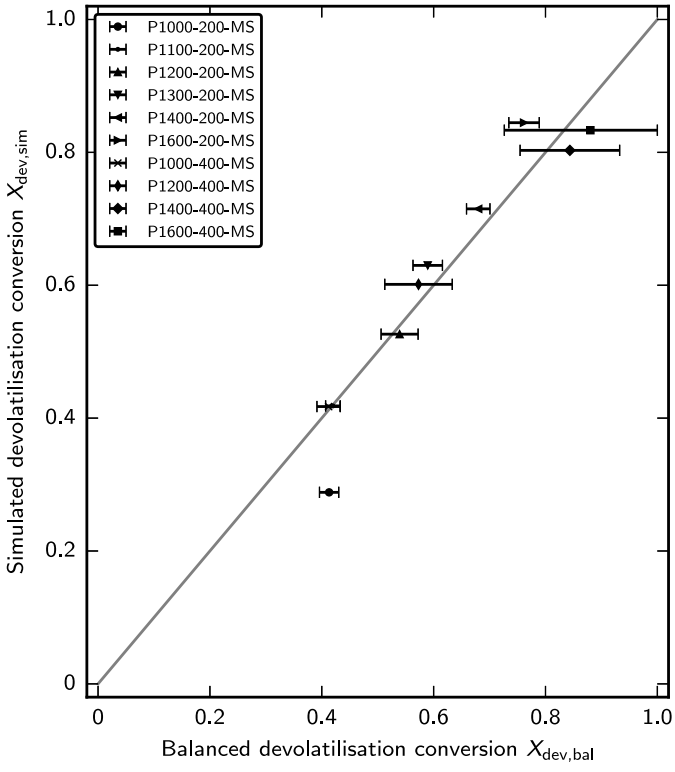

Fig. 10. Devolatilisation conversions simulated using the single first-order reaction Arrhenius law model $X_{dev,sim}$ in comparison with balanced devolatilisation conversions $X_{dev,bal}$.

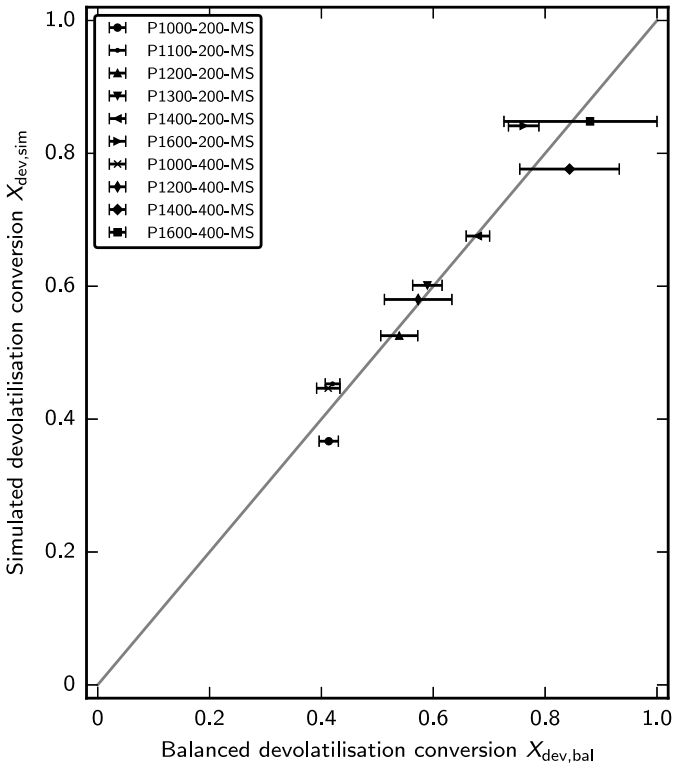

Fig. 11. Devolatilisation conversions simulated using the modified Yamamoto model $X_{dev,sim}$ in comparison with balanced devolatilisation conversions $X_{dev,bal}$.

Table 5
Parameters and coefficients of determination R^2 for the devolatilisation kinetics based on the single first-order reaction Arrhenius law model (SFORALM), the modified Yamamoto model (MYM) and the single first-order reaction Arrhenius law model (SFORALM) of Stösser [15] alongside the ranges of relative deviations (RD) between balanced and simulated devolatilisation conversions.

Model	$\frac{k_0}{1/s}$	$\frac{\overline{E}_a}{J/mol}$	C_1	C_2	C_3	R^2	$\frac{RD}{\%}$
SFORALM	266	48 232	–	–	–	0.891	−30.2 … 10.9
MYM	4511	64 724	1.010	−10.623	9.065	0.939	−11.2 … 10.5
SFORALM [15]	6400	72 000	–	–	–	–	–

conversions after the end of the second heating zone are also significant for larger particles that do no achieve the maximum possible conversion in the second heating zone. Thus, devolatilisation before and after the iso-thermal zones of drop-tube reactors should be accounted in the analysis.

4. Discussion

This section is focussed on the comparison of the TG and the DTR kinetics and links the measured gas species concentrations with the volatiles composition.

4.1. Comparison of TG kinetics and DTR kinetics

Zero-dimensional single-particle simulations were performed using an in-house software in Python and considering three test cases to

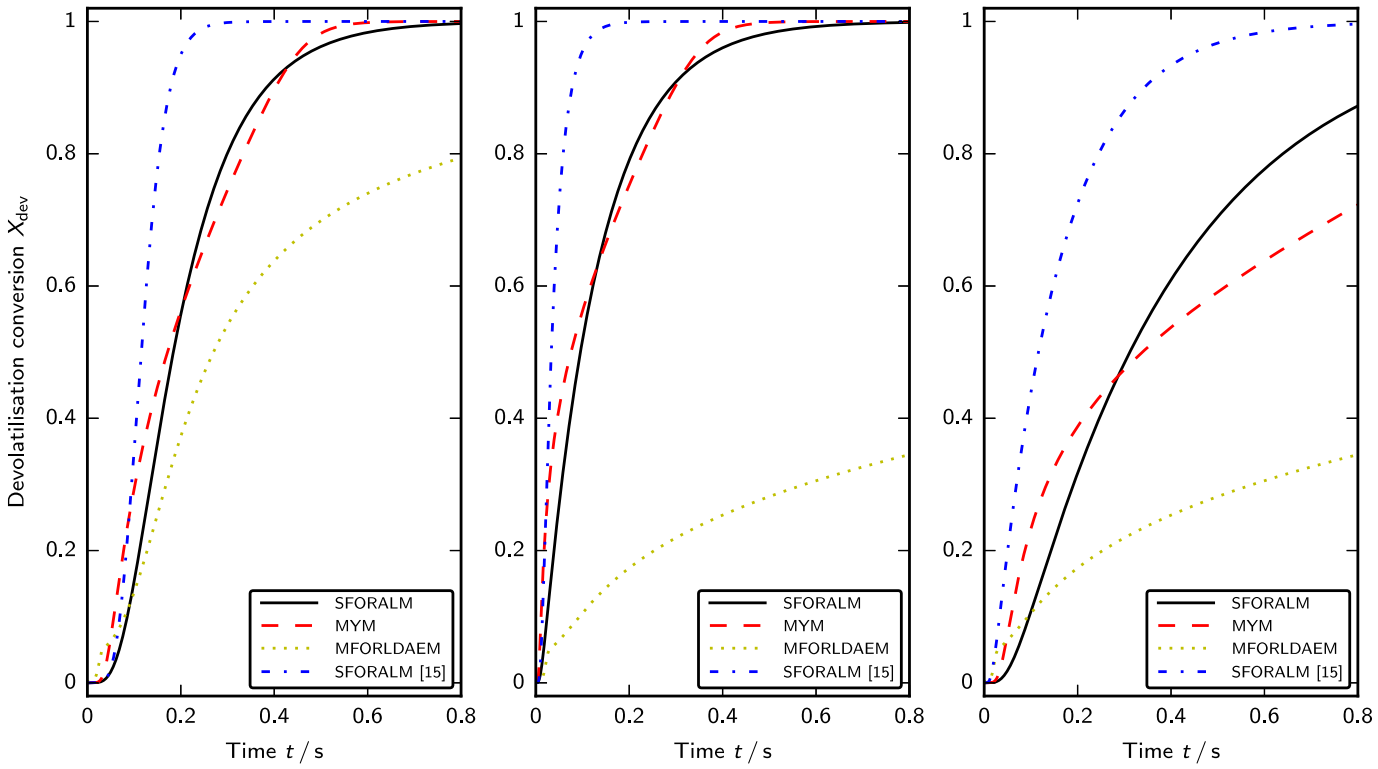

Fig. 12. Predicted devolatilisation conversions X_{dev} using the single first-order reaction Arrhenius law model (SFORALM), the modified Yamamoto model (MYM), the multi first-order reaction logistic distribution activation energy model (MFORLDAEM) and the single first-order reaction Arrhenius law model (SFORALM) of Stoesser [15] for test case 1 (left), test case 2 (centre) and test case 3 (right).

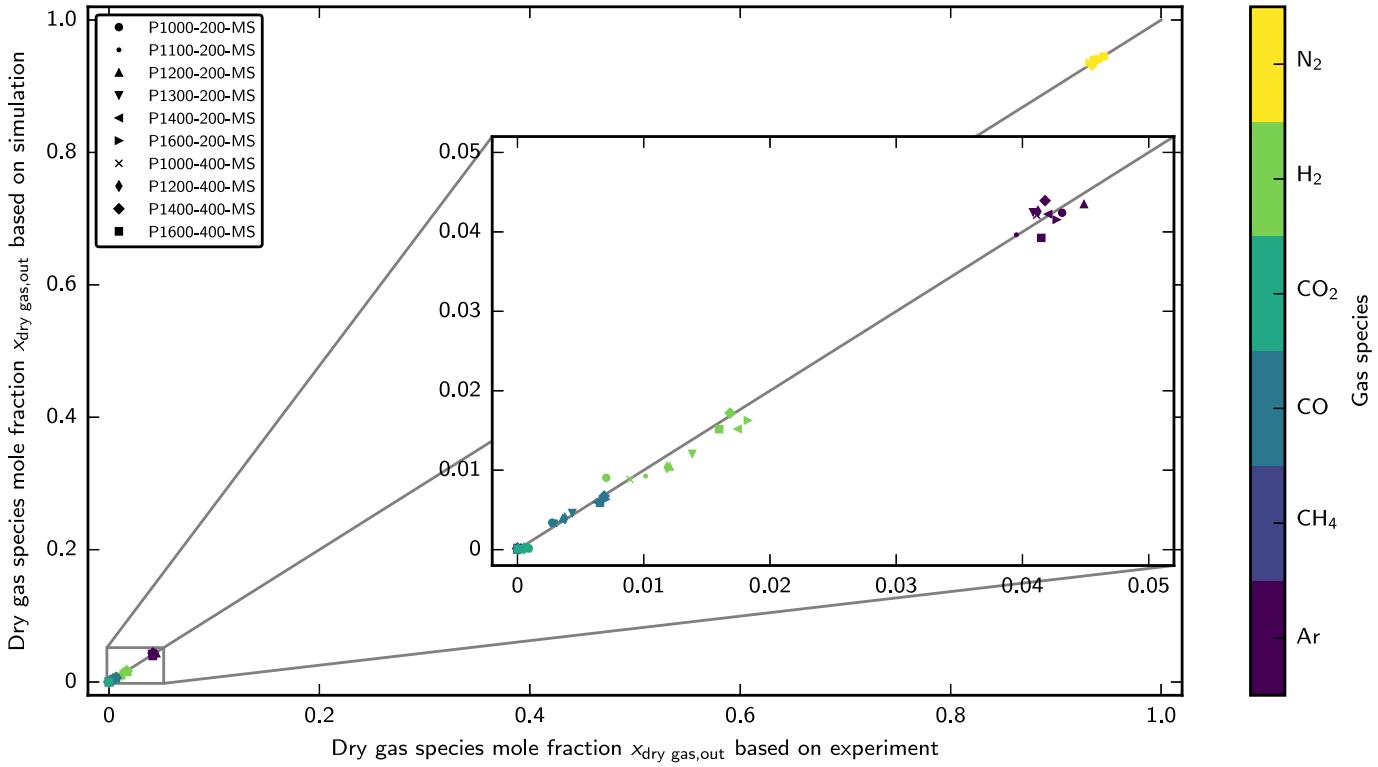

Fig. 13. Simulated measured dry gas species mole fractions at outlet in comparison with measured dry gas species mole fractions at outlet.

Table 6
Simulated devolatilisation conversions $X_{dev,sim}$ of the DTR experiments at various distances from the dosing tube inlet.

Experiment	$X_{dev,sim}$ (SFORALM)			$X_{dev,sim}$ (MYM)		
	810 mm	1730 mm	2750 mm	810 mm	1730 mm	2750 mm
P1000-200-MS	0.00	0.14	0.29	0.01	0.27	0.37
P1100-200-MS	0.01	0.23	0.42	0.03	0.35	0.45
P1200-200-MS	0.01	0.31	0.53	0.06	0.41	0.53
P1300-200-MS	0.02	0.41	0.63	0.08	0.48	0.60
P1400-200-MS	0.03	0.50	0.72	0.12	0.55	0.68
P1600-200-MS	0.06	0.66	0.85	0.19	0.68	0.84
P1000-400-MS	0.03	0.29	0.42	0.08	0.33	0.45
P1200-400-MS	0.06	0.50	0.60	0.17	0.46	0.58
P1400-400-MS	0.13	0.69	0.80	0.27	0.67	0.78
P1600-400-MS	0.26	0.73	0.83	0.39	0.75	0.85

Table 7
Initial particle diameters $d_{part,0}$, initial particle temperatures $T_{part,0}$ and gas temperatures T_{gas} of the test cases.

Test case	$d_{part,0}$ / µm	$T_{part,0}$ / K	T_{gas} / K
1	150	300	1673
2	50	300	1673
3	150	300	1273

compare the TG kinetics with the DTR kinetics. Differential particle transport equations were solved using the models and methods that were already used for the preceding single-particle simulations (see Section 2.7.1), using a constant specific particle heat capacity of 2000 J/(kg K) and a constant time step of 10^{-4} s. In test case 1, an initially non-moving spherical particle with an initial particle temperature of 300 K and an initial particle diameter of 150 µm is considered in a stationary non-moving gas consisting of nitrogen with a gas temperature of 1673 K at a constant pressure of 1 bar. In test case 2, the initial particle diameter is reduced to 50 µm. In test case 3, the gas temperature is decreased to 1273 K. The initial particle diameters $d_{part,0}$, the initial particle temperatures $T_{part,0}$ and the gas temperatures T_{gas} of the test cases are summarised in Table 7.

The predicted devolatilisation conversions X_{dev} are shown in Fig. 12. Accordingly, both DTR kinetics provide similar predictions for 1673 K although larger deviations can be found for shorter residence times due to the numerical optimisation in the absence of experimental data for such conditions (see Section 3.6). Significant deviations can also be found for the predictions based on the TG kinetics. At 800 ms, devolatilisation based on the DTR kinetics is almost finished for the test cases 1 and 2 while approximately 20% of the volatiles have still to be released according to the predictions based on the TG kinetics. Furthermore, the deviations strongly increase for lower gas temperatures. In test case 3, devolatilisation has progressed at 800 ms twice as fast if it is based on the DTR kinetics rather than on the TG kinetics. Thus, the TG kinetics provide lower devolatilisation conversion estimates, which could be connected with the experimental and numerical approach (i. e. measurements at low heating rates, approximation using the multi first-order reaction logistic distributed activation energy model and extrapolation to high-heating rates). In particular, the extrapolation could be afflicted with uncertainties. However, this needs further investigation. Meanwhile, the TG kinetics based on multi first-order reaction logistic distribution activation energy models are able to provide meaningful minimum devolatilisation conversion predictions. In contrast, TG kinetics based on multi first-order reaction Arrhenius law models provide less reliable and inferior extrapolation results as they do not account for distributed activation energies. Furthermore, the predictions based on the TG kinetics also show an increased gas release at the beginning of the conversion. This gas release reflects the humidity that was evaporated in the first stages of the TG analyses.

4.2. Comparison of beech wood char kinetics and fir char kinetics

Devolatilisation kinetics based on a single first-order reaction Arrhenius law model (SFORALM) were previously [15] developed for fir char using DTR experiments and are the only devolatilisation kinetics for biogenic chars at high-temperature conditions available to the best knowledge of the authors. The kinetic parameters are reproduced in Table 4 and strongly deviate from the parameters of the single first-order reaction Arrhenius law model for beech wood char. This is connected with the natural origin, the different pre-treatment methods and the assumptions used for the derivation of the kinetics. Specifically, the fir char differs in morphology and oxygen and volatiles contents compared to beech wood char. For example, the oxygen and volatiles mass fractions are twice as high. Furthermore, the kinetics were derived using simplified gas and particle conditions. As conversion before and after the second heating zone was neglected, the kinetics could overestimate the reaction rates.

For further analysis, zero-dimensional single-particle simulations were performed using the DTR kinetics for fir char and considering the three test cases from Section 4.1. The kinetics only were changed while using the same constant physical particle properties in order not affect the particle temperature predictions. The predicted devolatilisation conversions X_{dev} are shown in Fig. 12. The devolatilisation based on the DTR kinetics for fir char is approximately five-times faster than based on the DTR kinetics for beech wood char. This demonstrates the impact of the model assumptions and the chemical and physical properties. Therefore, customised devolatilsation kinetics should be developed for different wood chars using the most appropriate modelling approaches for DTR experiments. TG analyses may be used as a first approximation to compare the reaction rates of different wood chars.

4.3. Average volatiles composition

Gas species concentrations of the volatiles are an essential input for devolatilisation models in both combustion and gasification. Previous studies on coal entrained flow gasification [54–56] assumed that theoretical oxygenated and nitrogenated hydrocarbons $C_xH_yO_zN_w$ either decompose or react with O_2 and H_2O to CH_4, CO, CO_2, H_2, H_2O and N_2 while the volatiles composition was defined using elemental balances. Other studies applied not further specified equilibrium calculations [57, 58] or more detailed break-up approaches, for example, for black liquor decomposition [59–61] and for coal decomposition [62–64].

In addition to numerical estimates, gas species concentrations measurements are available from biomass pyrolysis experiments. Recently, Ontyd et al. [65] compared gas species concentrations measurements from fluidised-bed reactor and drop-tube reactor experiments with the predictions of the empirical model of Neves et al. [66]. At temperatures between 623 K and 1300 K, the fractions of H_2O and CO_2 generally decreased with increasing temperature while the fractions of CO and CH_4 increased [66]. H_2O was the major product at lower temperatures while CO was mainly found at higher temperatures [66], which is in agreement with typical equilibrium trends.

The dry gas species concentrations that were obtained in the DTR experiments are unfortunately affected by secondary gas reactions and do not reflect the instantaneous volatiles concentrations. Therefore, several attempts were made to determine an average volatiles composition using plug-flow-reactor simulations. Firstly, axial profiles of gas temperature and devolatilisation conversion were taken from the CFD simulations to provide the basis for reactive plug-flow reactor simulations with the GRI mechanism (version 3.0) [67] and with instantaneous mixing of carrier gas stream and secondary gas stream at the beginning of the second heating zone. Subsequently, a numerical optimisation was performed using an in-house software based on Python and Cantera [36] to determine an average volatiles composition that complies with the elemental balances. For the optimisation, the residuals were defined using the predicted and the measured dry gas

Table 8
Volatiles compositions in mass fractions $\boldsymbol{w}_{vol}$ and in mole fractions $\boldsymbol{x}_{vol}$.

i	$w_{i,vol}$	$x_{i,vol}$
CH_4	0–0.02	0–0.01
CO	0.75–0.81	0.26–0.27
CO_2	0–0.06	0-0.01
H_2	0.14–0.15	0.70–0.71
H_2O	0	0
N_2	0.02	0.01

species concentrations at the outlet of the DTR. Furthermore, the mass fractions of two volatiles species were regarded as independent parameters, while the mass fractions of the other volatiles species were fixed by the elemental composition of the primary wood char and the elemental balances. The predicted and measured dry gas species concentrations are compared in Fig. 13, demonstrating that the optimisation was able to provide meaningful results for the dry gas species concentrations at the outlet despite strong model simplifications. The estimated ranges for the average volatiles compositions in mole and mass fractions are given in Table 8. The predicted values indicate that the average volatiles composition at high-heating-rate and high-temperature conditions is close to the equilibrium volatiles composition at high temperatures. Thus, the latter can be a good estimate in the absence of experimental data.

5. Conclusions

Thermogravimetric analyses and drop-tube reactor experiments were performed with primary beech wood char (commercially produced at 800-900 K) under inert conditions to derive devolatilisation kinetics for the design and scale-up of entrained flow gasification processes. Kinetics based on a single first-order reaction Arrhenius law model, a modified Yamamoto model and a multi first-order reaction logistic distribution activation energy model were established and subsequently compared using single-particle simulations. The results demonstrated that the predictions based on the drop-tube reactor kinetics are in good agreement with each other within the validity limits, while deviations were found outside the limits at short residence times. The results also showed that predictions based on the thermogravimetric kinetics underpredict the conversion at high-heating-rate and high-temperature conditions. However, the thermogravimetric kinetics based on a distributed activation energy model are able to provide good estimates in the absence of elaborative drop-tube reactor kinetics. This assumes that the thermogravimetric analysis data can be reproduced with good accuracy when facing fluctuating fuel properties and applying small sample sizes. Furthermore, the dry gas species concentrations from the drop-tube reactor experiments were used to estimate an average volatiles composition. The optimisation results indicated that the average volatiles composition is close to the equilibrium volatiles composition at high temperature conditions.

CRediT authorship contribution statement

Maximilian Dammann: Writing – original draft, Writing – review & editing, Visualization, Validation, Software, Methodology, Investigation, Formal analysis, Conceptualization. **Stella Clara Walker:** Writing – review & editing, Validation, Methodology, Investigation, Conceptualization. **Marco Mancini:** Writing – review & editing, Supervision. **Thomas Kolb:** Writing – review & editing, Supervision, Project administration, Funding acquisition.

Declaration of competing interest

The authors declare that they have no known competing financial interests or personal relationships that could have appeared to influence the work reported in this paper.

Data availability

Data will be made available on request.

Acknowledgements

The authors thank (i) the Helmholtz Association of German Research Centres (HGF) for funding the programmes Energy Efficiency, Materials and Resources (EMR) and Materials and Technologies for the Energy Transition (MTET), (ii) Michael Schneider (formerly Karlsruhe Institute of Technology, Engler-Bunte-Institute, Combustion Technology), Philipp Stösser and Christoph Schneider (formerly Karlsruhe Institute of Technology, Engler-Bunte-Institute, Fuel Technology and Karlsruhe Institute of Technology, Institute for Technical Chemistry, Gasification Technology) for their preceding studies, (iii) Sabina Hug and Stefan Schneider (Karlsruhe Institute of Technology, Engler-Bunte-Institute, Fuel Technology), Klaus Hirsch and Astrid Huber (Karlsruhe Institute of Technology, Institute of Mechanical Process Engineering and Mechanics) and Volker Zibat (Karlsruhe Institute of Technology, Light Technology Institute) for their experimental support.

Supplementary material

Supplementary material related to this article can be found online at https://doi.org/10.1016/j.fuel.2024.131967.

References

[1] ISO Organization for Standardization. 1994, ISO 10780:1994-11. Stationary source emissions: Measurement of velocity and volume flowrate of gas streams in ducts.
[2] Dahmen N, Abeln J, Eberhard M, Kolb T, Leibold H, Sauer J, et al. The bioliq process for producing synthetic transportation fuels, WIREs Energy and Environment 6 (3). http://dx.doi.org/10.1002/wene.236.
[3] Nikrityuk P, Meyer B, editors. Gasification processes: Modeling and simulation. Weinheim, Germany: Wiley-VCH; 2014.
[4] Mularski J, Pawlak-Kruczek H, Modlinski N. A review of recent studies of the CFD modelling of coal gasification in entrained flow gasifiers, covering devolatilization, gas-phase reactions, surface reactions, models and kinetics. Fuel 2020;271:117620. http://dx.doi.org/10.1016/j.fuel.2020.117620.
[5] Dammann M. Numerical modelling and simulation of atmospheric entrained flow gasification of surrogate fuels [Ph.D. thesis], Karlsruhe, Germany: Fakultät für Chemieingenieurwesen und Verfahrenstechnik, Karlsruher Institut für Technologie; 2024, http://dx.doi.org/10.5445/IR/1000172116.
[6] Di Blasi C. Combustion and gasification rates of lignocellulosic chars. Prog Energy Combust Sci 2009;35(2):121–40. http://dx.doi.org/10.1016/j.pecs.2008.08.001.
[7] Niksa S. Predicting the rapid devolatilization of diverse forms of biomass with bio-flashchain. Proc Combust Inst 2000;28(2):2727–33. http://dx.doi.org/10.1016/s0082-0784(00)80693-1.
[8] Niksa S. Bio-FLASHCHAIN® theory for rapid devolatilization of biomass. 1. Lignin devolatilization. Fuel 2020;263:116649. http://dx.doi.org/10.1016/j.fuel.2019.116649.
[9] Niksa S. Bio-FLASHCHAIN® theory for rapid devolatilization of biomass. 2. Predicting total yields for torrefied woods. Fuel 2020;263:116645. http://dx.doi.org/10.1016/j.fuel.2019.116645.
[10] Niksa S. Bio-flashchain® theory for rapid devolatilization of biomass. 3. Predicting total yields for torrefied grasses and agricultural residues. Fuel 2020;263:116646. http://dx.doi.org/10.1016/j.fuel.2019.116646.
[11] Biagini E, Falcitelli M, Tognotti L. Devolatilisation and pyrolysis of biomasses: Development and validation of structural models. In: Proceedings of the XXIX meeting of the Italian Section of the Combustion Institute, 14-17 June 2006, Pisa, Italy. Pisa, Italy: Italian Section of the Combustion Institute; 2006.
[12] Chen Y, Charpenay S, Jensen A, Wójtowicz MA, Serio MA. Modeling of biomass pyrolysis kinetics. Symp (International) Combust 1998;27(1):1327–34. http://dx.doi.org/10.1016/s0082-0784(98)80537-7.
[13] De Jong W, Di Nola G, Venneker BCH, Spliethoff H, Wójtowicz. TG-FTIR pyrolysis of coal and secondary biomass fuels: Determination of pyrolysis kinetic parameters for main species and NO_x precursors. Fuel 2007;86(15):2367–76. http://dx.doi.org/10.1016/j.fuel.2007.01.032.
[14] Stoesser P, Schneider C, Kreitzberg T, Kneer R, Kolb T. On the influence of different experimental systems on measured heterogeneous gasification kinetics. Appl Energy 2018;211:582–9. http://dx.doi.org/10.1016/j.apenergy.2017.11.037.

[15] Stösser P. Investigation of solid-phase processes during the conversion of biogenic slurry in entrained-flow gasifiers. [Ph.D. thesis], Karlsruhe, Germany: Fakultät für Chemieingenieurwesen und Verfahrenstechnik, Karlsruher Institut für Technologie; 2020.

[16] Schneider C, Stoesser P, Rincon S, Kolb T. Determination of heterogeneous reaction kinetics of high-temperature biomass char. In: Proceedings of the 28th Deutscher Flammentag: Verbrennung und Feuerung, 6-7 September 2017, Darmstadt, Germany, Vol. 2161 of VDI-Berichte, Deutsche Vereinigung für Verbrennungsforschung and The Combustion Institute Deutsche Sektion. VDI-Verlag, Düsseldorf, Germany; 2017, p. 331–43.

[17] Schneider C, Zeller M, Böhm D, Kolb T. Influence of pressure on the gasification kinetics of two high-temperature beech wood chars with CO_2, H_2O and its mixture. Fuel 2021;299:120523. http://dx.doi.org/10.1016/j.fuel.2021.120523.

[18] Simone M, Biagini E, Galletti C, Tognotti L. Evaluation of global biomass devolatilization kinetics in a drop tube reactor with CFD aided experiments. Fuel 2009;88(10):1818–27. http://dx.doi.org/10.1016/j.fuel.2009.04.032.

[19] Niemelä NP, Tolvanen H, Saarinen T, Leppänen A, Joronen T. CFD based reactivity parameter determination for biomass particles of multiple size ranges in high heating rate devolatilization. Energy 2017;128:676–87. http://dx.doi.org/10.1016/j.energy.2017.04.023.

[20] Johansen JM, Gadsbøll R, Thomsen J, Jensen PA, Glarborg P, Ek P, et al. Devolatilization kinetics of woody biomass at short residence times and high heating rates and peak temperatures. Appl Energy 2016;162:245–56. http://dx.doi.org/10.1016/j.apenergy.2015.09.091.

[21] Johansen JM, Jensen PA, Glarborg P, Mancini M, Weber R, Mitchell RE. Extension of apparent devolatilization kinetics from thermally thin to thermally thick particles in zero dimensions for woody biomass. Energy 2016;95:279–90. http://dx.doi.org/10.1016/j.energy.2015.11.025.

[22] Johansen JM, Jensen PA, Glarborg P, De Martini N, Ek P, Mitchell RE. High heating rate devolatilization kinetics of pulverized biomass fuels. Energy Fuels 2018;32(12):12955–61. http://dx.doi.org/10.1021/acs.energyfuels.8b03100.

[23] Branca C, Di Blasi C. Global kinetics of wood char devolatilization and combustion. Energy Fuels 2003;17(6):1609–15. http://dx.doi.org/10.1021/ef030033a.

[24] Holzkohleverarbeitung Schütte. 2021, [link] URL http://www.holzkohleverarbeitung-schuette.de/.

[25] Eberhard M, Santo U, Michelfelder B, Günther A, Weigand P, Matthes J, et al. The bioliq® Entrained Flow Gasifier: A model for the German Energiewende. ChemBioEng Rev 2020;7(4):106–18. http://dx.doi.org/10.1002/cben.202000006.

[26] Schneider C, Walker S, Phounglamcheik A, Umeki K, Kolb T. Effect of calcium dispersion and graphitization during high-temperature pyrolysis of beech wood char on the gasification rate with CO_2. Fuel 2021;283:118826. http://dx.doi.org/10.1016/j.fuel.2020.118826.

[27] DIN Deutsches Institut für Normung. 2007, DIN 51732:2007-08. Prüfung fester Brennstoffe. Bestimmung des Gesamtgehaltes an Kohlenstoff, Wasserstoff und Stickstoff. Instrumentelle Methoden.

[28] DIN Deutsches Institut für Normung. 2012, DIN 51724-3:2012-07. Prüfung fester Brennstoffe. Bestimmung des Schwefelgehaltes. Teil 3: Instrumentelle Verfahren.

[29] DIN Deutsches Institut für Normung. 1997, DIN 51719:1997-07. Prüfung fester Brennstoffe. Bestimmung des Aschegehaltes.

[30] DIN Deutsches Institut für Normung. 2002, DIN 51718:2002-06. Prüfung fester Brennstoffe. Bestimmung des Wassergehaltes und der Analysenfeuchtigkeit.

[31] DIN Deutsches Institut für Normung. 2001, DIN 51720:2001-03. Prüfung fester Brennstoffe. Bestimmung des Gehaltes an Flüchtigen Bestandteilen.

[32] DIN Deutsches Institut für Normung. 2003, DIN 51900-2:2003-03. Prüfung fester und flüssiger Brennstoffe. Bestimmung des Brennwertes mit dem Bomben-Kalorimeter und Berechnung des Heizwertes. Teil 2: Verfahren mit isoperibolem oder static-jacket Kalorimeter.

[33] Eurofins Umwelt Ost. 2021, [link] URL https://www.eurofins.de/.

[34] DIN Deutsches Institut für Normung. 2011, DIN EN 15104:2011-04. Feste Biobrennstoffe. Bestimmung des Gesamtgehaltes an Kohlenstoff, Wasserstoff und Stickstoff. Instrumentelle Verfahren.

[35] DIN Deutsches Institut für Normung. 2011, DIN EN 15289:2011-04. Feste Biobrennstoffe. Bestimmung des Gesamtgehaltes an Schwefel und Chlor.

[36] Goodwin DG, Speth RL, Moffat HK, Weber BW. Cantera: An object-oriented software toolkit for chemical kinetics, thermodynamics and transport processes. 2021, http://dx.doi.org/10.5281/zenodo.4527812, https://www.cantera.org, version 2.5.1.

[37] Stoesser P, Ruf J, Gupta R, Djordjevic N, Kolb T. Contribution to the understanding of secondary pyrolysis of biomass-based slurry under entrained-flow gasification conditions. Energy Fuels 2016;30(8):6448–57. http://dx.doi.org/10.1021/acs.energyfuels.6b00935.

[38] MathWorks. 2019, MATLAB. Release 2019b.

[39] Cai J, Wu W, Liu R. An overview of distributed activation energy model and its application in the pyrolysis of lignocellulosic biomass. Renew Sustain Energy Rev 2014;36(2014):236–46. http://dx.doi.org/10.1016/j.rser.2014.04.052.

[40] Anthony DB, Howard JB, Hottel HC, Meissner HP. Rapid devolatilization of pulverized coal. Symp (International) Combust 1975;15(1):1303–17. http://dx.doi.org/10.1016/s0082-0784(75)80392-4.

[41] Várhegyi G, Szabó P, Antal MJ. Kinetics of charcoal devolatilization. Energy Fuels 2002;16(3):724–31. http://dx.doi.org/10.1021/ef010227v.

[42] Miura K, Maki T. A simple method for estimating f(E) and k0(E) in the distributed activation energy model. Energy Fuels 1998;12(5):864–9. http://dx.doi.org/10.1021/ef970212q.

[43] Miura K. A new and simple method to estimate f(E) and k0(E) in the distributed activation energy model from three sets of experimental data. Energy Fuels 1995;9(2):302–7. http://dx.doi.org/10.1021/ef00050a014.

[44] Yamamoto K, Murota T, Okazaki T, Taniguchi M. Large eddy simulation of a pulverized coal jet flame ignited by a preheated gas flow. Proc Combust Inst 2011;33(2):1771–8. http://dx.doi.org/10.1016/j.proci.2010.05.113.

[45] Richards AP, Fletcher TH. A comparison of simple global kinetic models for coal devolatilization with the CPD model. Fuel 2016;185:171–80. http://dx.doi.org/10.1016/j.fuel.2016.07.095.

[46] Di Blasi C. Influences of physical properties on biomass devolatilization characteristics. Fuel 1997;76(10):957–64. http://dx.doi.org/10.1016/s0016-2361(97)00096-3.

[47] Hindmarsh AC. ODEPACK, a systematized collection of ODE solvers. IMACS Trans Sci Comput 1983;1:55–64.

[48] Petzold L. Automatic selection of methods for solving stiff and nonstiff systems of ordinary differential equations. SIAM J Sci Stat Comput 1983;4(1):136–48. http://dx.doi.org/10.1137/0904010.

[49] Virtanen P, Gommers R, Oliphant TE, Haberland M, Reddy T, Cournapeau D, et al. SciPy 1.0 Contributors, SciPy 1.0: Fundamental algorithms for scientific computing in Python. Nature Methods 2020;17:261–72. http://dx.doi.org/10.1038/s41592-019-0686-2.

[50] SciPy Developers. SciPy. Release 1.5.1. 2021, URL https://pypi.org/project/scipy/.

[51] Morin M, Pécate S, Masi E, Hémati M. Kinetic study and modelling of char combustion in TGA in isothermal conditions. Fuel 2017;203:522–36. http://dx.doi.org/10.1016/j.fuel.2017.04.134.

[52] Janse AMC, de Jonge HG, Prins W, van Swaaij WPM. Combustion kinetics of char obtained by flash pyrolysis of pine wood. Ind Eng Chem Res 1998;37(10):3909–18. http://dx.doi.org/10.1021/ie970705i.

[53] Senneca O, Urciuolo M, Chirone R. A semidetailed model of primary fragmentation of coal. Fuel 2013;104:253–61. http://dx.doi.org/10.1016/j.fuel.2012.09.026.

[54] Kumar M, Ghoniem AF. Multiphysics simulations of entrained flow gasification. Part II: Constructing and validating the overall model. Energy Fuels 2012;26(1):464–79. http://dx.doi.org/10.1021/ef2008858.

[55] Vascellari M, Arora R, Pollack M, Hasse C. Simulation of entrained flow gasification with advanced coal conversion submodels. Part 1: Pyrolysis. Fuel 2013;113:654–69. http://dx.doi.org/10.1016/j.fuel.2013.06.014.

[56] Halama S, Spliethoff H. Numerical simulation of entrained flow gasification: Reaction kinetics and char structure evolution. Fuel Process Technol 2015;138:314–24. http://dx.doi.org/10.1016/j.fuproc.2015.05.012.

[57] Watanabe H, Otaka M. Numerical simulation of coal gasification in entrained flow coal gasifier. Fuel 2006;85(12–13):1935–43. http://dx.doi.org/10.1016/j.fuel.2006.02.002.

[58] Ku X, Li T, Løvås T. Eulerian-Lagrangian simulation of biomass gasification behavior in a high-temperature entrained-flow reactor. Energy Fuels 2014;28(8):5184–96. http://dx.doi.org/10.1021/ef5010557.

[59] Marklund M. Pressurized entrained-flow high temperature black liquor gasification: CFD based reactor scale-up method and spray burner characterization [Ph.D. thesis], Luleå, Sweden: Department of Engineering Sciences and Mathematics, Luleå University of Technology; 2006, https://nbn-resolving.org/urn:nbn:se:ltu:diva-26275.

[60] Marklund M, Tegman R, Gebart R. CFD modelling of black liquor gasification: Identification of important model parameters. Fuel 2007;86(12–13):1918–26. http://dx.doi.org/10.1016/j.fuel.2006.12.015.

[61] Marklund M, Tegman R, Gebart R. A self-consistent CFD-model for pressurised high temperature black liquor gasification. IFRF Combust J 200801, https://ifrf.net/research/archive/a-self-consistent-cfd-model-for-pressurised-high-temperature-black-liquor-gasification.

[62] Syamlal M, Bissett LA. METC gasifier advanced simulation (MGAS) model. Tech. Rep., Morgantown, WV, USA: U.S. Department of Energy, Office of Fossil Energy; 1992, http://dx.doi.org/10.2172/10127635.

[63] Kumar U, Salem AM, Paul MC. Investigating the thermochemical conversion of biomass in a downdraft gasifier with a volatile break-up approach. Energy Procedia 2017;142:822–8. http://dx.doi.org/10.1016/j.egypro.2017.12.132.

[64] Kumar U, Paul MC. CFD modelling of biomass gasification with a volatile break-up approach. Chem Eng Sci 2018;195(2019):413–22. http://dx.doi.org/10.1016/j.ces.2018.09.038.

[65] Ontyd C, Pielsticker S, Yildiz C, Schiemann M, Hatzfeld O, Ströhle J, et al. Experimental determination of walnut shell pyrolysis kinetics in N_2 and CO_2 via thermogravimetric analysis, fluidized bed and drop tube reactors. Fuel 2021;287:119313. http://dx.doi.org/10.1016/j.fuel.2020.119313.

[66] Neves D, Thunman H, Matos A, Tarelho L, Gómez-Barea A. Characterization and prediction of biomass pyrolysis products. Prog Energy Combust Sci 2011;37(5):611–30. http://dx.doi.org/10.1016/j.pecs.2011.01.001.

[67] Smith GP, Golden DM, Frenklach M, Moriarty NW, Eiteneer B, Goldenberg M, et al. GRI-Mech 3.0. 1999, URL http://combustion.berkeley.edu/gri-mech/.